Motion-Artifact Resistant Design of Photoplethysmograph Ring Sensor for Driver Monitoring

by

Honghui Jiang

B.S Mechanical Engineering (2002)
University of Michigan

Submitted to the Department of Mechanical Engineering
In Partial Fulfillment of the Requirement for the Degree of

Master of Science in Mechanical Engineering

at the

Massachusetts Institute of Technology

Feb, 2004

Signature redacted

Signature of Author.....
Department of Mechanical Engineering
Dec 14, 2003

Signature redacted

Certified by.....
Haruhiko Harry Asada
Ford Professor of Mechanical Engineering
Thesis Supervisor

Signature redacted

Accepted by.....
Ain A. Sonin
Chairman, Department Committee on Graduate Students

Motion-Artifact Resistant Design of Photoplethysmograph Ring Sensor for Driver Monitoring

by

Honghui Jiang

Submitted to the Department of Mechanical Engineering on Dec 14, 2003
In Partial Fulfillment of the Requirement for the Degree of
Master of Science in Mechanical Engineering

Abstract

Through extensive literature search, it has been found that there exists strong correlation between the *Mental Workload* of an automobile driver with his or her physiological measurements, especially the Heart Rate Variability (HRV) measurements. In order to make a driver's HRV monitoring on the road possible, a new photoplethysmograph (PPG) Ring Sensor prototype has been devised specifically for countering the problem of motion artifact that almost all wearable PPG sensors are facing. Most importantly, the motion artifacts on PPG signals caused by motion in the direction of blood flow in the digital arteries along the finger flanks have been eliminated using a customized Adaptive Noise Cancellation algorithm. Both the lab results and the road test results have suggested that the new Ring Sensor is indeed capable of rejecting motion artifacts in all three possible motion axes and producing considerable amount of usable beat-to-beat heart rate data on the road for HRV analysis. The problem of occasional missing data on the road has also been tackled with a suitable linear curve-fitting algorithm. Also, the sunlight saturation problem is dealt with using a simple DC averaging reference circuit. The final road test has proven the validity of the driver *Mental Workload* model and the validity of the Ring Sensor in monitoring the HRV of the driver on the road. Besides the application on driver monitoring, the Ring Sensor can also be used for other forms of wearable monitoring such as jogging.

Thesis Supervisor: Haruhiko H. Asada
Title: Professor of Mechanical Engineering

TABLE OF CONTENTS

TABLE OF FIGURES

1 THE IMPORTANCE OF DRIVER MONITORING

Various analyses and comprehensive studies [1][2][3] have shown that human errors are the sole cause in around 60% of all automobile accidents and are a contributing factor in over 90%. Despite the fact that a considerable percentage of these errors are contributed by intentional driving behaviors (e.g. speeding, fail to stop at red light and etc.) [4], most other factors that lead to road accidents can be categorized in two major groups (based on factors analyzed in [5]): a) the worsening of a driver's mental condition and b) the increase in a driver' task workload.

Crucial mental conditions of the driver include alertness, calmness and concentration on the road. For example, the lack of alertness due to drowsiness led to 56,000 crashes and 1,550 fatalities in US in 1996 [6]. On the other hand, Type A Behavior Pattern (competitive achievement orientation, sense of urgency, anger/hostility and etc.), Trait-Anxiety (both physical and emotional symptoms of nervousness) and Cognitive Failure (everyday slips and lapses) contribute directly to the loss of calmness and concentration of automobile drivers. These have been shown to have strong correlations with road traffic accidents [5].

Increase in a drivers' task workload is the result of complexity of the traffic environment (e.g. unfamiliarity with the road, heavy traffic) and the increasing amount of tasks to be handled on the driving panel with the introduction of new in-car systems (e.g. stereo, cell phone, collision warning system, adaptive cruise control and GPS). This leads to the driver being overloaded and distracted, and thus causes accidents due to drivers being unable to respond to sudden changes in the road conditions [5][7][8].

2 DRIVER'S MONITORING BASED ON HEART RATE VARIABILITY

2.1 A Driver's Mental Condition and Workload

Since drivers' mental conditions and workload have been proven to be associated with the occurrence of road accidents, it is essential that some kind of sensory systems can help to detect this before it is too late. Dr. Dick de Waard from the Center for Environmental and Traffic Psychology at the University of Groningen has published an extensive research paper [8] in 1996 on the different ways to measure the mental condition and workload of drivers. It has been shown that many online and offline measurement are capable of indicating symptoms of bad mental conditions and task overloading of drivers. The following figure summarizes some of the experimental results.

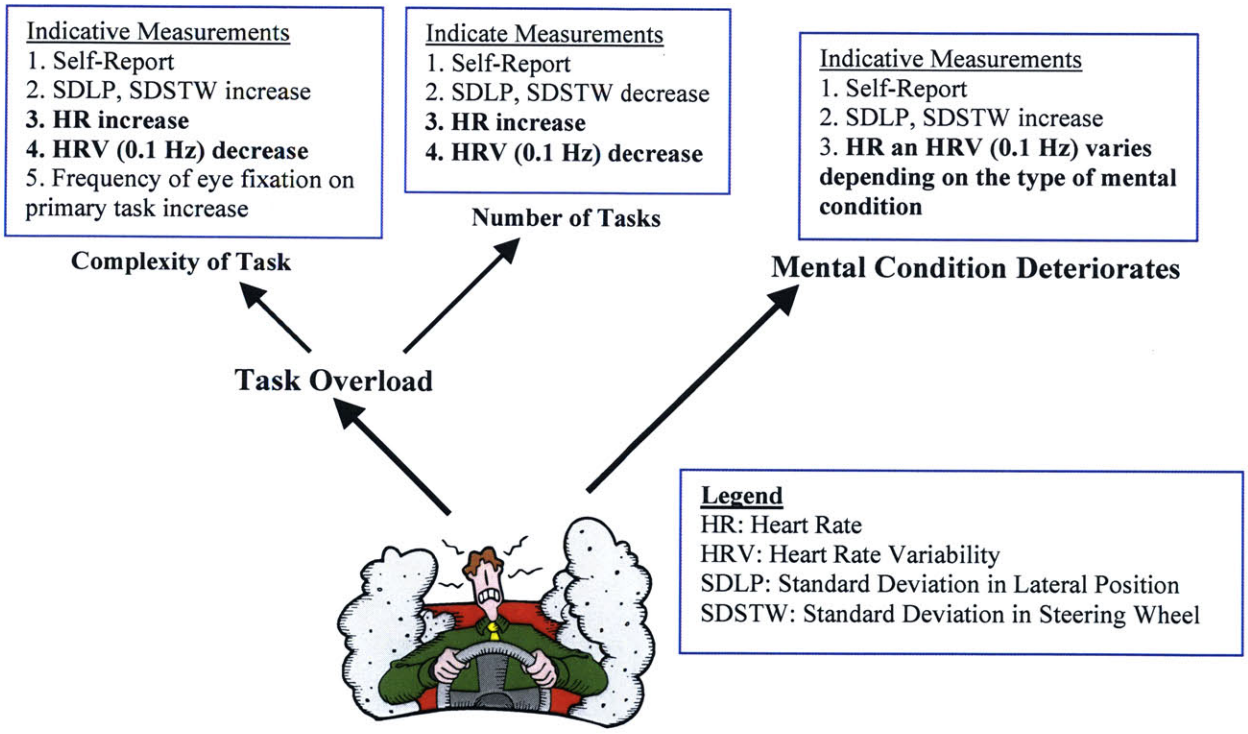

Figure 2-1: Various measurements that indicate mental condition deterioration and task overload

It is clear from the above figure that both offline evaluation (self-report) and real time evaluation (SDLP, SDSTW, HR, HRV and eye fixation) can be used to access the mental conditions of the

drivers and whether they are overloaded by driving related tasks. In fact, from the driver's point of view, the increase in the task workload and decrease in mental condition are essentially the same [8] and can be viewed collaboratively as an increase in *Perceived Mental Workload* (referred to as *Mental Workload* in the rest if the thesis). The following figure summarizes this fact and graphically displays the various measurements that can indicate the region of performance of the driver.

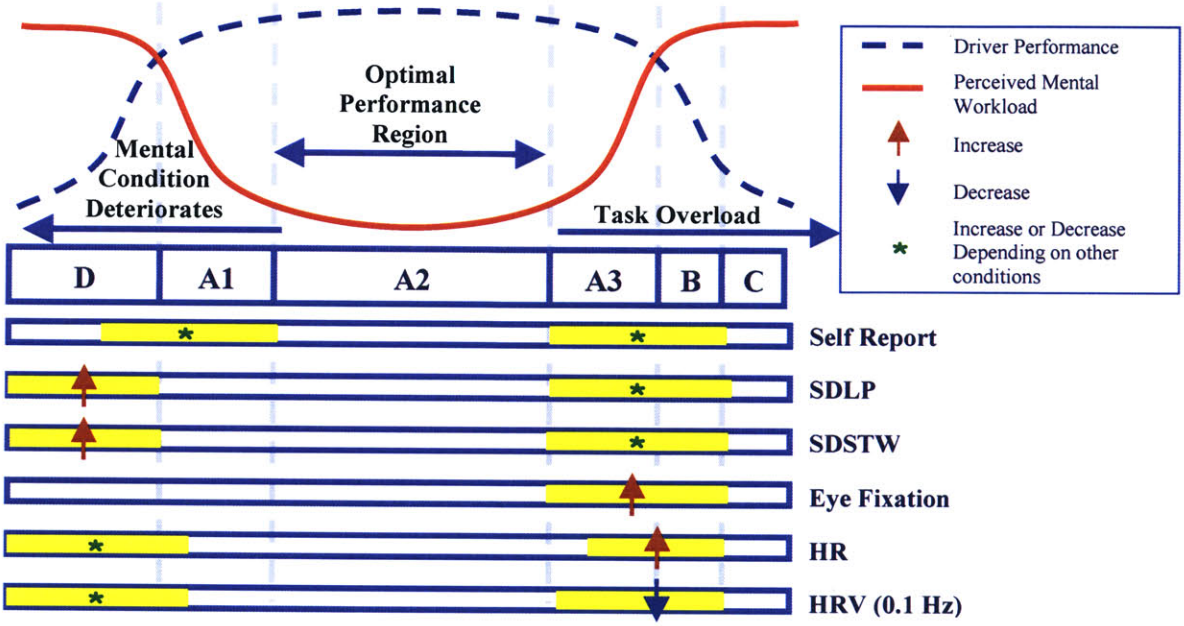

Figure 2-2: Measurements indicating the different driver performance and perceived workload region

A2 is the optimal performance region where the driver is experiencing the least amount of *Mental Workload* and the performance is the best. Both A1 and A3 are the transition region to unacceptable driver performance. The driver is experiencing an increasing amount of *Mental Workload* and is trying to keep up with the performance by exerting extra mental effort. Region D, B and C are where the driver can no longer cope with the excessive increase in *Mental Workload* and performance starts to deteriorate significantly. This is when accidents usually occur.

Although the above figures suggest that any single measurement is not sufficient to characterize the region of performance of the driver, a combination of a few of those measurements is indeed capable of indicating the *Mental Workload* of the driver. The measurements presented above are not an exhaustive list of all the possible measurements. However, these are indeed the ones that can be most conveniently monitored and measured (e.g. brain wave measurement using EEG can detect certain driving behavior but it is nearly impossible to do it in the actual driving scenario).

2.2 Heart Rate (HR) and Heart Rate Variability (HRV)

2.2.1 The Importance of HR and HRV in Indicating Change in *Mental Workload*

With the advance in sensor technology, it is relatively easy to obtain measurement readings that are associated with the vehicle (such as SDLP and SDSTW mentioned Figures 1 and 2), and it has even become possible to monitor the eye fixation and facial expression of the driver through advanced video monitoring and processing technology. However, instrumentation on the vehicle can only signal either increases or decreases and is thus unable to differentiate between the many mental conditions of the driver. On the other hand, video monitoring tends to signal false indications. For example, frowning can reflect the complexity of the road condition, but can also be because of a glimpse of thought of some unhappy incidents the driver experienced earlier in the day. Therefore, there is a need for some more objective and highly correlated measurements.

The physiological states (e.g. heart rate, heart rate variability, blood pressure and etc.) of a person are such kinds of measurements, and it has also been shown that the correlation of these measurements to the change in *Mental Workload* varies relatively slightly (based on analysis of variance of experimental results) among different persons [8]. Both Figure 2-1 and Figure 2-2 have indicated that heart rate (HR) and heart rate variability (HRV) are correlated with the change in *Mental Workload* of the drivers. Besides the extensive discussion in paper [8] by Dr. Dick De Waard, other research papers [9] [10] [11] [12] have also demonstrated the correlation of HR and HRV with various mental conditions that have direct effect on a driver's performance (especially fatigue, drowsiness, stress and frustration). Therefore, the ability to measure accurately the HR and HRV of a driver in real time is highly valuable for determining his or her *Mental Workload.*

2.2.2 Definitions for HR and HRV and Their Correlation with Mental Conditions

HR is defined as the rate of pumping of the heart, and in most of the biomedical applications average HR is used to monitor a person's health condition. On the other hand, HRV is defined as the variation of the *beat-to-beat* HR and is often presented in the frequency domain as a power spectrum. The unit used on the x-axis is usually Hz instead of rad/sec for many other power spectrum analyses. Therefore, in order to accurately measure the HRV, the rate of every single heartbeat becomes essential.

The analysis on HR is simple as only an increase and decrease is signified and correlated with mental conditions. However HRV is analyzed in different frequency bands and each band corresponds differently to the change in mental conditions. In normal practice, HRV is characterized in three major frequency bands.

Table 2-1: The different frequency band for HRV and the mental activities associated

Freq. Band	Freq. Range	Mental Activities Associated
LF	0.01-0.08Hz	Mainly sympathetic activities (stress/frustration)
MF	0.08-0.15Hz	Mixed sympathetic and parasympathetic activities
HF	0.15-0.50Hz	Respiratory sinus arrhythmia and is almost exclusively due to parasympathetic activity

Based on these definitions, it has been shown through ANOVA (analysis of variance) on experimental data the following correlations between HRV and various mental conditions.

Table 2-2: Correlation of HRV and HR with various mental conditions (N.S.C. = Not Strongly Correlated)

Mental Condition	LF	MF	HF	LF/HF	MF/(LF+HF)	HR
Joyful/Relaxed	N.S.C.	Increase	N.S.C.	Increase	N.S.C.	Decrease
Anger/Stress	Increase	N.S.C.	N.S.C.	N.S.C.	Increase	Increase
Fatigue/Drowsiness	Increase	Increase	Decrease			Decrease

Based on the correlation results from the above table and results from Figure 2-1 and Figure 2-2, it is clear that HRV and HR are associated with all kinds of changes of *Mental Workload*. The

actual real-time road driving test on these correlations are not performed due to the complexity of the current setup for HRV measurement (complicated and clumsy ECG equipment that is very difficult to wear while driving), and the high sensitivity of ECG measurement to muscular movement that is common on the road. Therefore, ECG is not applicable for driver monitoring. Nevertheless, the simulated lab environments that these experimental tests are based on are convincing enough that with the possibility of wearable HRV/HR sensors (together with other vehicle sensors mentioned in the previous session), we can closely monitor the *Mental Workload* of the driver, and thus be able to give warning prior to accidents happening. The following sections will focus on the development of such a device, which is named the Ring Sensor.

3 RING SENSOR DESIGN FOR HEART RATE VARIABILITY MEASURMENT

3.1 Working Principle of Ring Sensor

The Ring Sensor is an innovative sensor device that measures photoplethysmograph (PPG) signals at the base of a human finger. The initial development of this device is discussed in the journal paper published by H. Harry Asada, Phillip Shaltis, Andrew Reisner, Sokwoo Rhee and Reginald Hutchinson in IEEE Transaction on Biomedical Engineering [13]. Figure 3-1 shows the typical waveform of a PPG signal obtained from a human subject *at rest.* The signal comprises a large segment of DC signal and a small amplitude AC signal. The DC component of photon absorption results from light passing through various non-pulsatile media, including tissue, bones, venous blood, and non-pulsatile arterial blood. Fluctuation of DC components might happen if light path is disturbed or the arterial blood level being altered. This will result in DC noise affecting the AC component and thus destroying the pulsatile waveform. In order to get HR/HRV information using the Ring Sensor, it is crucial to get as perfect a PPG waveform as possible. This is especially true for HRV measurement because beat-to-beat HR depends solely on the time lapse between subsequent pulses' peaks, which correspond to the systolic points in the cardiovascular cycles.

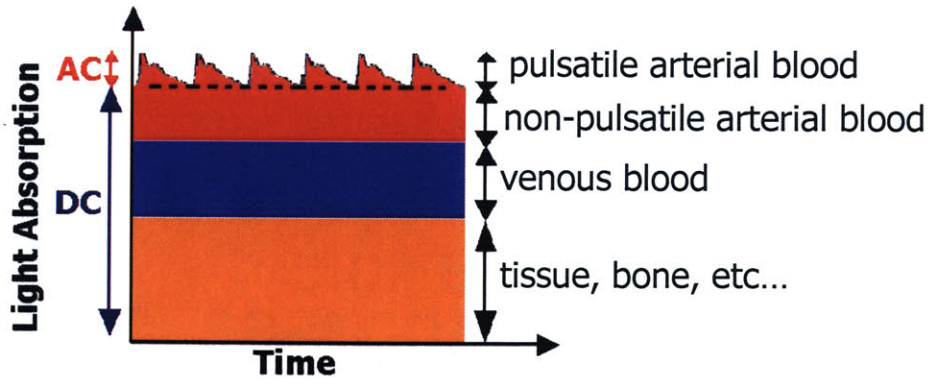

Figure 3-1: Illustrative representation of the relative photon absorbance for various sections of the finger. The DC component is significantly larger than the AC component. [13]

The Ring Sensor uses a light-emitting diode (LED) and a photodiode (PD) for detecting the PPG waveform. The locations of the LED and the PD relative to the finger are an important design issues determining signal quality and robustness against various kinds of disturbances (mainly

motion artifacts). Therefore, the LED and PD are placed on the flanks of the finger base rather than the dorsal and palmar sides. These locations are desirable for two reasons:

- Both flanks of the finger have a thin epidermal tissue layer through which photons can reach the target blood vessels with less attenuation
- The digital arteries are located near the skin surface parallel to the length of the finger.
- The finger base has the least amount of motion under any finger movement

Getting PPG signals from the digital arteries is essential, because an arterial pulsation is not only greater in magnitude than cutaneous pulsations, but is also less susceptive to motion due to the naturally higher internal pressure. While the capillaries collapse with small external pressures on the order of 10~30 mmHg, the arteries can sustain external pressures up to 70~80 mmHg [13]. Figure 4 shows the cross-sectional views of the finger with the two possible sensor locations: a) reflective setup (LED and PD on the same side of the finger), b) transmittal setup (LED and PD on opposite sides of the finger)

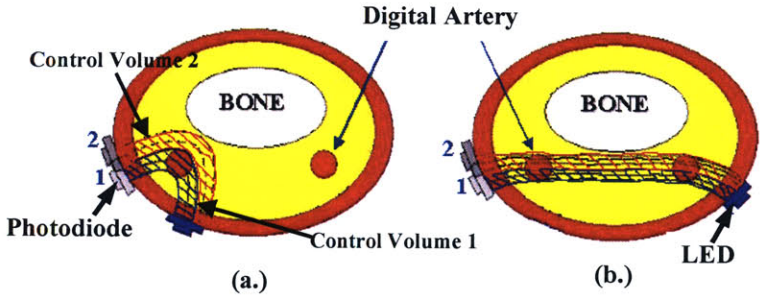

Figure 3-2: (a) For the reflective illumination method, movement of the photo diode relative to the LED (position 1 to position 2) leads to a photo path that no longer contains the digital artery. (b) For the transmittal illumination method, movement of the photodetector relative to the LED still contains photon paths that pass through the digital artery. [13]

From the above figure, it is clear that the reflective signals will suffer significantly from small sensor location shift (from 1 to 2), because the amount of light absorbed by the DC component (tissue, non-pulsatile blood and etc.) changes as the light path changes. This makes the reflective configuration sensitive to motion artifact. On the other hand, although transmittal setup is much less affected by small sensor location change (from 1 to 2), the longer light path that travels through the finger makes the signal quality highly dependent on many factors that might alter or even cut the path (e.g. deformation of finger under external pressure). Also, the transmittal setup

requires much higher light intensity to penetrate through the entire finger base. Therefore, in order to draw a conclusion on which type of sensor setup to use, extensive experiments were conducted to compare closely the pros and cons of the two setups.

3.2 Comparison of Transmittal and Reflective PPG Signals

Since the small shifts of sensor location due to hand motion cause the major drawback of the reflective sensor setup, the sensors were taped to the finger base to ensure no relative motion between the finger skin and the sensors. Similarly, the LED was adjusted to its maximum intensity to ensure the amount of light penetration needed for the transmittal signal. By doing these two adjustments, the comparison between the two sensor locations is believed to be impartial and judicial. Figure 3-3 shows the comparisons of reflectance signals and transmittance signals taken on the same finger base simultaneously under the above experimental condition.

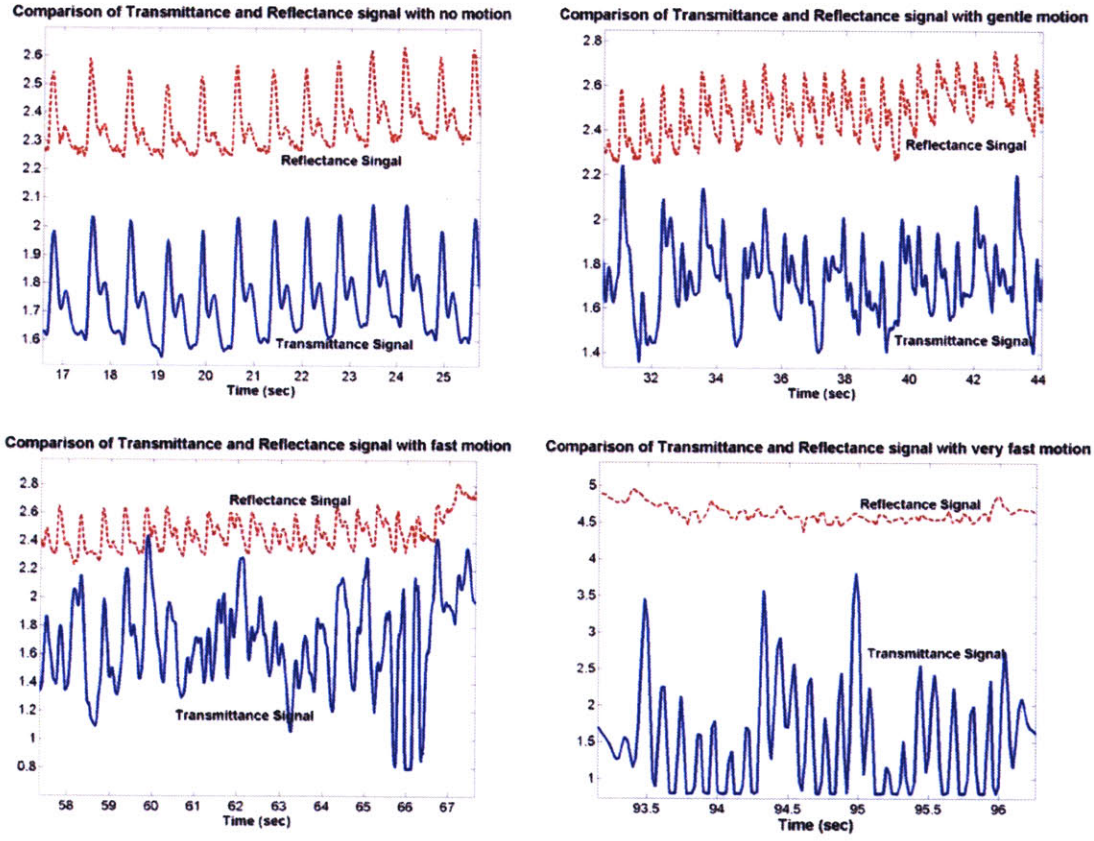

Figure 3-3: Comparison of Transmittance and Reflectance PPG signals under 4 different motion settings: a) No motion, b) Gentle motion (<0.5G acceleration), c) Fast motion (0.5-1G acceleration) and d) Very fast motion (>1G acceleration). The motion applied is through lateral hand shaking perpendicular to the blood flow.

It is clearly shown by these comparisons that reflectance PPG signals are better than transmittance PPG signals once the problem of relative motion between the sensor head and skin is solved. This is because with the LED and PD having firm contact with the skin at all time, the light path that travels through the reflective setup is barely affected by motion. So, there is much less fluctuation of the DC component in the reflectance PPG signal, and thus the AC component to noise ratio is minimal. On the other hand, the long light path that the transmittance signal experiences makes its DC component very susceptible to any blood level changes or tissue shape changes along the path. Since the center part of the finger base is soft, continuous motion will cause it to be compressed and distorted. This affects both the tissue and the capillaries inside the finger base. These contribute to the large amount of DC component change in the transmittance signal as can be seen in Figure 3-3.

Based on the above experimental analysis, it is obvious that reflective sensor setup should be chosen. Nevertheless, Figure 3-3 does show that when the accelerations are too large, even the reflectance signal waveforms start to distort. This is most likely because the surface contact between the sensor head and the skin does not allow light to penetrate deep enough. The PD can therefore not fully capture the PPG signal from the digital arteries, which are much deeper inside the finger. When the motion starts to get larger, the surface capillaries from which most of the PPG signals are actually taken from start to collapse and no pulsatile waveform can be observed (the last graph in Figure 3-3 shows this effect). Therefore, further improvements are needed to ensure that the PD is getting signals mostly from the digital arteries, which do not collapse under normal motion.

3.3 Improvement on Reflectance PPG Signal with Local Pressure Mechanism

The reason why a simple surface contact between the sensor head and the skin is not sufficient to get a good amount of signal from the digital artery has to do with the transumural pressure of the digital artery. Transumural pressure is the pressure difference between the inside and outside of the blood vessel. The pulsatile amplitude of the arterial blood is at a maximum when the transumural pressure goes to zero due to the nonlinear compliance of the blood vessel [13]. Therefore, external pressure on the digital artery is needed in order to have the maximum arterial pulsatile signal. However, the pressure applied cannot be excessive because the amplitude will

decrease once the transumural pressure passes the zero point (see Figure 3-4), and also excessive pressure will cause damage over other vasculature [13]. Neither can the pressure be applied across the entire finger base surface where the ring sensor is attached, as this will cause all base capillaries to collapse and will block the blood flow in and out of the finger. Thus, the pressure applied should be local and must be adjustable.

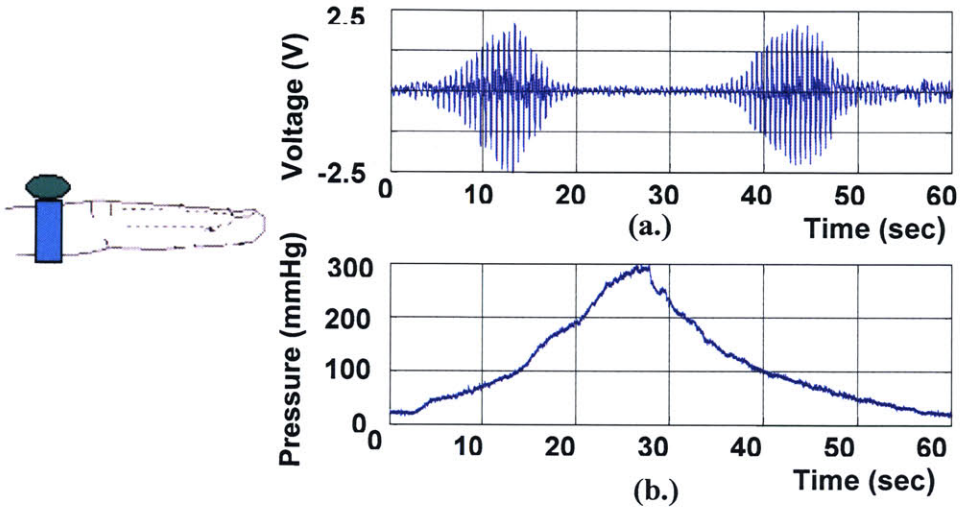

Figure 3-4: (a.) PPG signal amplitude (b.) Pressure at the photo detector [13]

Based on the above considerations, a new sensor band has been designed. It has a block of soft rubber pad to provide a local pressure at the sensor head near a digital artery. Also, by adjusting the tightness of the sensor band around the finger, the local pressure level can be adjusted. Figure 3-5 and 3-6 on the next page illustrates this concept.

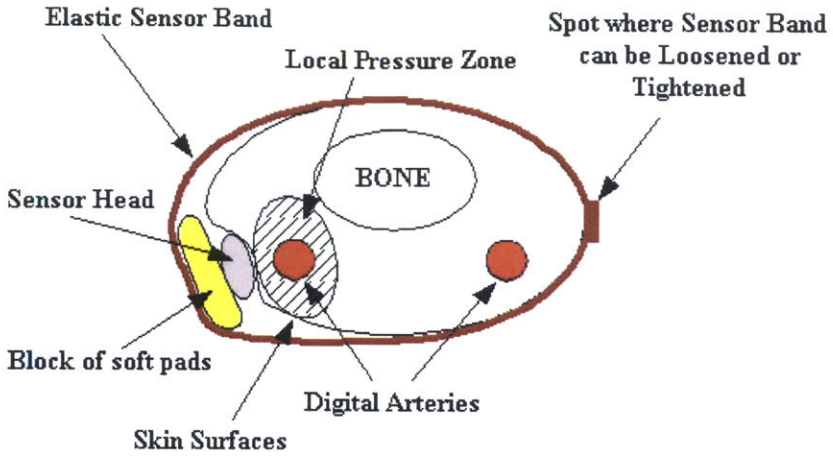

Figure 3-5: Modified sensor band for convenient build-in local pressure mechanism

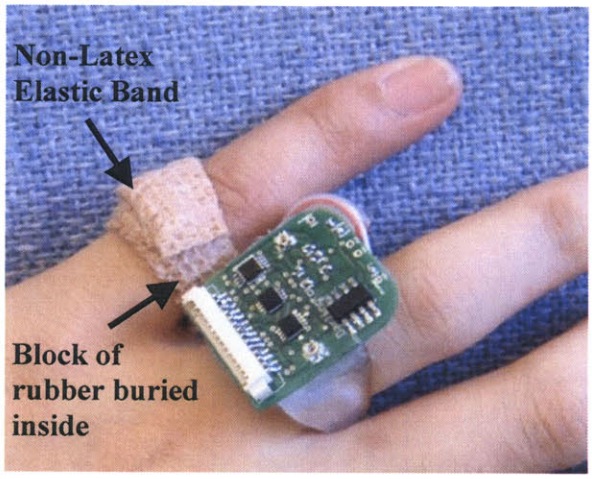

Figure 3-6: Picture of the actual Ring Sensor with sensor band worn on the same hand

In this setting, the local force applied on the sensor head by the rubber block is counter balanced by the force distributed along the skin surface on the opposite side of the finger. This allows a relatively large local pressure (around 70-80mmHg which is equal to the internal pressure of the digital artery) to be applied at the digital artery near the sensor head and having a small pressure (<<10mmHg) distributed over the rest of the finger surface. This ensures good signal output without causing any unwanted damage on the finger. Moreover, the elastic sensor band can be easily adjusted to maximize the comfort of wearing and ensure skin-sensor contact at all time.

The following experimental results show the success of such a local pressure mechanism in getting good PPG waveforms under motion artifacts of up to 3G acceleration (approximately $30m/s^2$). The accelerations are applied through lateral oscillations of the hand perpendicular to the digital arteries along the finger flanks, and the accelerations are measured using a MEMS accelerometer. Experimental data without the local pressure mechanism are also shown for comparison.

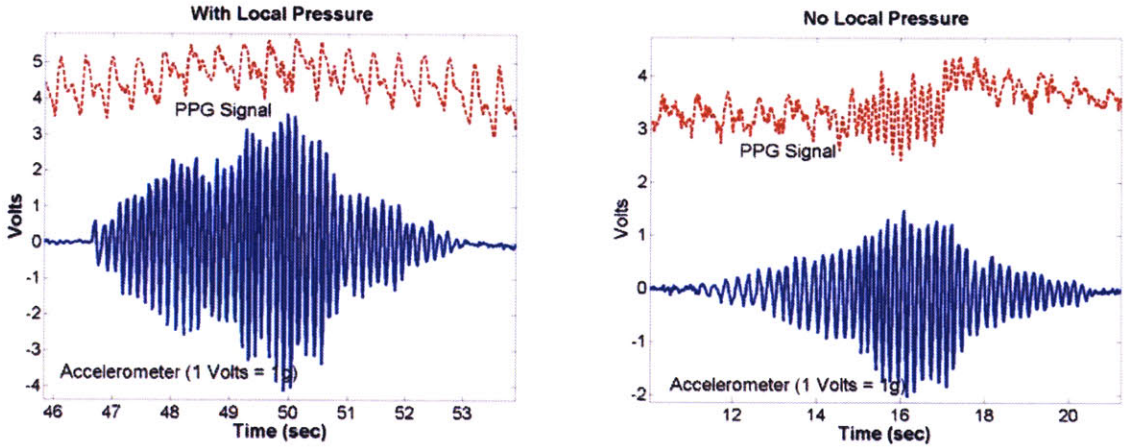

Figure 3-7: Comparison of PPG signal with and without local pressure mechanism (1V=1G for the accelerometer). Without local pressure mechanism the waveform start to distort at about 1G of acceleration.

It is clear from the above comparison that the local pressure mechanism greatly improves the signal quality under the influence of hand motion perpendicular to the arteries. However, the local pressure mechanism is a passive device and it only ensures that the PPG signal reading is mostly obtained from the digital arteries. Therefore, it cannot help to differentiate between a true PPG signal and a PPG signal that is corrupted with unwanted blood volume change caused by external motion. This unwanted volume change usually does not occur under normal circumstances when the applied external motion is perpendicular to the blood vessel. This explains why the local pressure works well for this type of motion. However, whenever there exists some motion along the blood vessel, a simple passive device becomes inadequate and a more advanced solution is needed.

4 Advanced Motion Artifact Reduction Using Adaptive Noise Cancellation

4.1 The Problem

With the local pressure mechanism at the sensor head, the motion disturbances in the directions perpendicular to the arteries in the fingers are rejected for up to 3G ($30m/s^2$) of acceleration. This is because the local pressure zone makes the transmural pressure at the digital arteries close to zero and thus allows maximum PPG signal to be read. Moreover, at 3G of acceleration, the digital arteries do not collapse. This ensures true readings of the blood volume inside the arteries throughout the period that the sensor is attached. Furthermore, the blood volume changes due to perpendicular motion are relatively small compared to that caused by the pulse wave sent down by every heartbeat. Therefore, the PPG signal obtained from the improved Ring Sensor reflects mostly the pulsatile blood volume change even with motion disturbances perpendicular to digital arteries in the fingers.

However, there is a type of hand motion that will cause the blood volume in the digital artery to change considerably without causing any artery collapses. This is the motion along the direction of blood flow in the digital arteries along the finger flanks. The following figure illustrates this motion type and defines the axis notation for the analysis that follows.

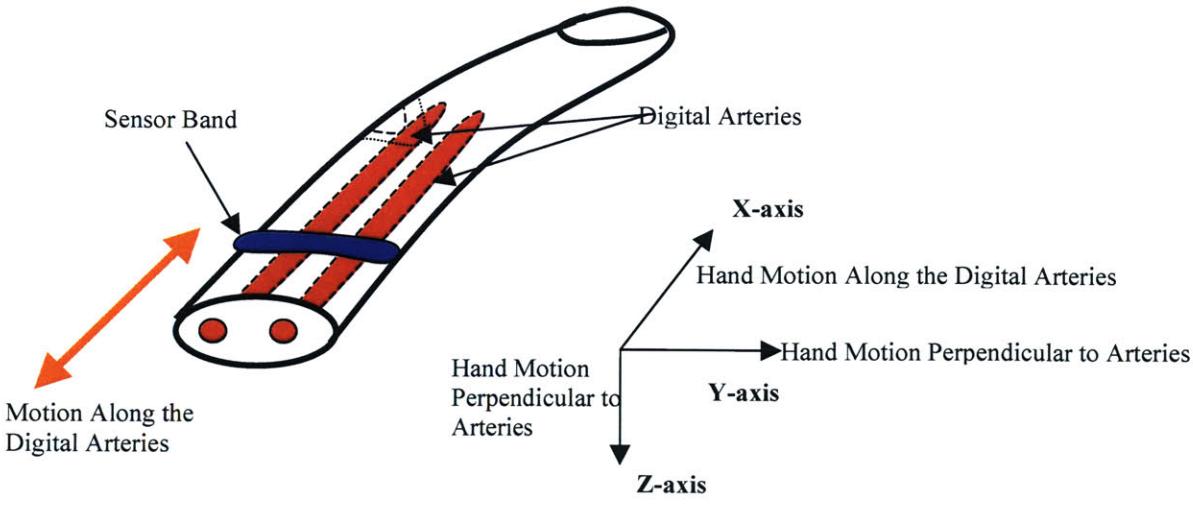

Figure 4-1: Illustration of hand motion type and axis definition for motion analysis

Based on the definition of the three axes, it can be summarized at this point that the Y-axis and Z-axis motion are mostly rejected with the local pressure mechanism for up to 3G of acceleration as discussed earlier. However, the X-axis motion causes large disturbances in the PPG signal even with the local pressures. This is because motion along the digital artery will cause the blood to move up and down along the blood vessels. This dynamic blood movement is unstoppable and causes dynamic changes in the blood volume, which leads to dynamic disturbances in the PPG signal. Figure 4-2 shows the PPG signal under X-axis motion and what the correct PPG should look like without the motion. The correct PPG is collected at the stationary right hand while the X-axis-motion-corrupted PPG is collected on the moving left hand. Accelerometer readings are attached to show the extent of oscillatory motion applied.

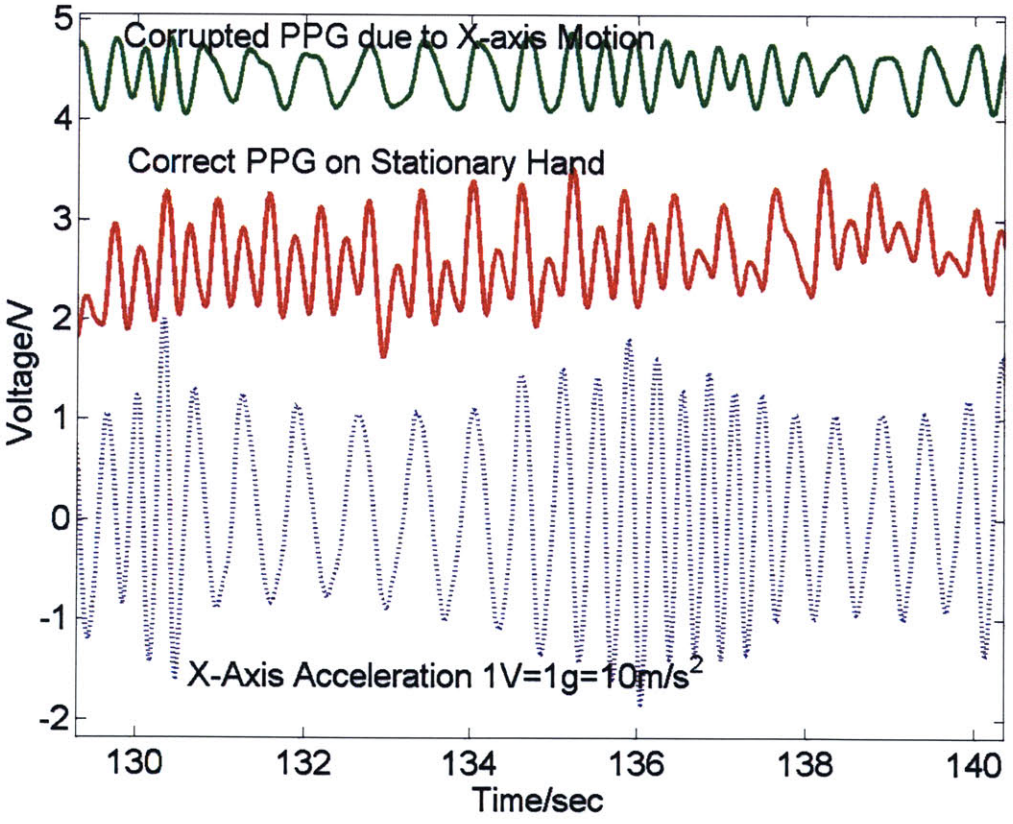

Figure 4-2: Corrupted PPG due to X-axis motion on the moving left hand; Correct PPG on the stationary right hand; and X-Axis acceleration monitored using MEMS accelerometer (for both PPG wave, voltage magnitude is scaled for clarity of illustration)

It can be seen from the above figure that, the X-axis acceleration totally deforms the PPG signal on the moving hand that was monitored, with the absolute magnitude of the X-axis acceleration between 1G and 2G. This shows that the PPG signals are very sensitive to X-axis motion due to the movement of the blood along the arteries. One interesting observation can be made out of the above figure: the frequency of the corrupted PPG signal seems to correspond closely with the frequency of the applied motion. This point will be made clear towards the later part of the thesis.

For the acceleration monitoring on the finger, a MEMS accelerometer was used and was attached to the Ring Sensor circuit board fastened on the same finger where the sensor band was located. The following two figures show an illustration of the attachment details and a picture of the actual setup.

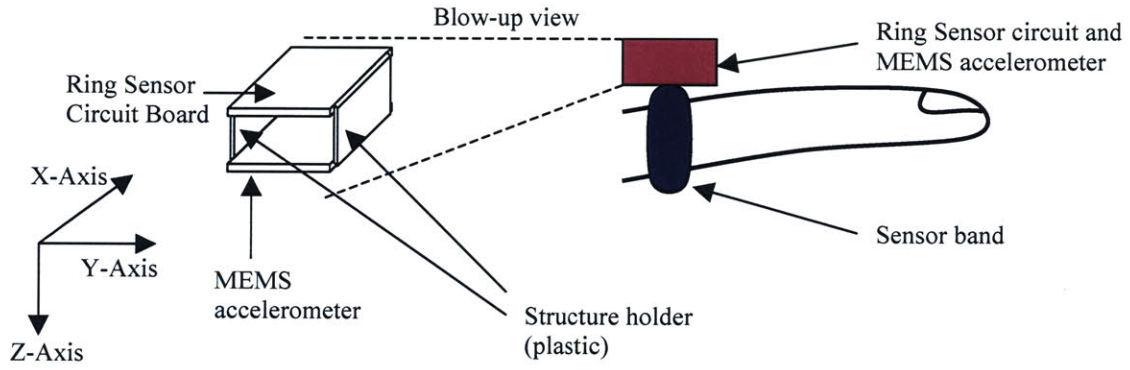

Figure 4-3: Illustration of the MEMS accelerometer attachment relative to the Ring Sensor and finger

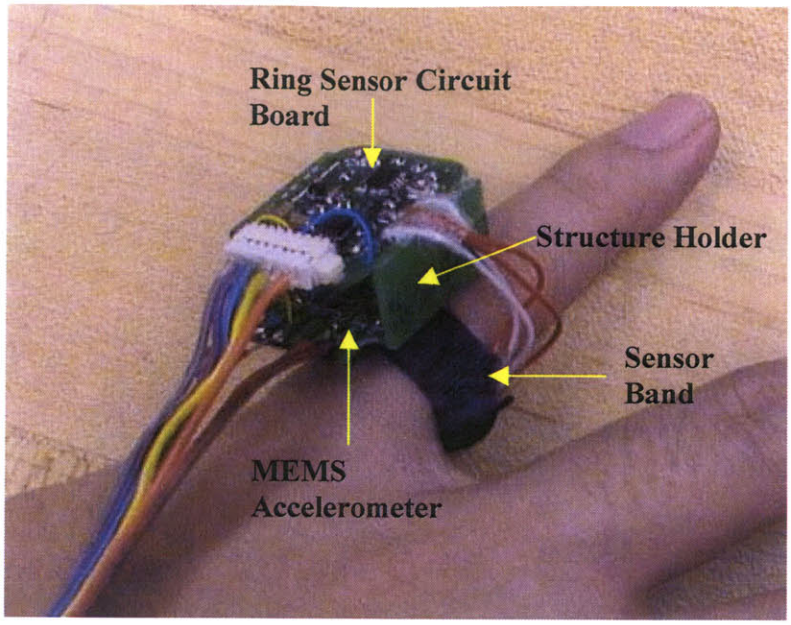

Figure 4-4: Picture of the actual attachment and setup

Due to the size limitation, the MEMS accelerometer that fits to the size of the Ring Sensor can only measure acceleration along the X and Y-axis. Nevertheless, this is more than sufficient as the problem with motion artifact arises mostly in the X-axis as long as the local pressure mechanism is enforced.

4.2 The Correlation Between Acceleration and Motion-disturbed PPG signal

As observed in Figure 4-2, there exists a correlation between the frequency of the X-axis acceleration and that of the corrupted PPG signal. Therefore, it is possible to model this corrupted signal as the system response to the X-axis acceleration. In this section, a discrete time model of this system will be derived and analyzed.

First of all, X-axis accelerations bring about blood displacements inside the digital arteries. Let x be the blood displacement and let a be the blood acceleration in the X-axis direction. For this discrete model, although a general Infinite Impulse Response (IIR) seems to be the most adequate representation of the actual continuous system, a Finite Impulse Response (FIR) model was chosen instead:

$$x_t = c_1 a_{t-1} + c_2 a_{t-2} + c_3 a_{t-3} + \cdots + c_n a_{t-n} \tag{4-1}$$

where, a_{t-n} represent the X-axis acceleration input at time t-n, and x_t is the x value at current time, t.

There are two reasons for choosing the FIR model and both of them will be further explored in a later section of this chapter. They are presented here to first support the model in Equation (4-1), as it will be used for further equation derivations. The two reasons are

- Firstly, the motion disturbance causes by the acceleration on the PPG signal has a fast rise and settling time. Therefore, the system does not need to be fitted with an infinite model
- Secondly, the FIR model is the best form that suits the Adaptive Noise Cancellation Algorithm for motion artifact rejection

With Equation (4-1) and the assumption that the blood vessel cross-section is uniform and fixed throughout the motion, we arrive at the following equation

$$\begin{aligned} V_t &= Sx_t = S(c_1 a_{t-1} + c_2 a_{t-2} + c_3 a_{t-3} + \cdots + c_n a_{t-n}) \\ \Rightarrow V_t &= p_1 a_{t-1} + p_2 a_{t-2} + p_3 a_{t-3} + \cdots + p_n a_{t-n} \end{aligned} \tag{4-2}$$

where V_t is the blood volume change at any instant time t due to X-axis motion, and S is the area of the cross-section. p_1 to p_n are the coefficients for the system FIR model.

Assuming that the magnitude change of a PPG signal is positively proportional to the blood volume change inside the blood vessel for the duration of the small time window of the FIR model, V_t in Equation (4-2) can be linearly transformed to represent the actual magnitude change of the PPG signal due to X-axis acceleration. Using y_t to represent the change in PPG magnitude, Equation (4-2) becomes:

$$y_t = q_1 a_{t-1} + q_2 a_{t-2} + q_3 a_{t-3} + \cdots + q_n a_{t-n} \tag{4-3}$$

This y_t can also be viewed as the motion artifacts caused by the X-axis accelerations on the PPG signal.

In order to verify this model and determine the number of model coefficients to use (the value of n), correlation analyses were performed between the y data series and the a data series obtained in actual experiments using the sensor setup mentioned in the previous section. The sampling

rate was set at 1000 samples/sec. Because only the actual X-axis-motion-corrupted PPG signal is obtained, the y series can only be estimated by subtracting the correct PPG on the stationary hand away from the corrupted PPG on the moving hand. Denoting the actual corrupted PPG data series by r_t and the correct PPG data series by k_t, we have

$$y_t = r_t - k_t \tag{4-4}$$

In this subtraction, the following assumptions are made

- The changes in the magnitude of the PPG signal due to X-axis motion and due to heartbeat are assumed to be additive
- The correct PPG signal obtained on the stationary right hand is assumed to be equal to the correct PPG signal that would have been obtained from the moving left hand if it were stationary

Furthermore, to analyze the dynamic system response (rise and settling time) to X-axis acceleration, several additional y data series were created with time delays that were multiples of +0.01s from the original y data series. For example, y data series having no time delay represent the data series ($y_t, y_{t+1} \ldots y_{t+m}$) and y data series having +0.05s (50 sample points) time delay represents the data series ($y_{t+50}, y_{t+51} \ldots y_{t+50+m}$). The a data series, ($a_t, a_{t+1} \ldots a_{t+m}$), does not have delay at all. The correlations between the a data series and each delayed y data series were performed. Through delaying the y series and doing the correlation with the a series, the exact time instant of the system's peak response to X-axis acceleration can be determined.

The formula used for calculating the correlation index is as follows.

$$Correlation(y,a) = \frac{1}{m} \frac{\sum (y_i - \mu_y)(a_i - \mu_a)}{\sigma_y \sigma_a} \tag{4-5}$$

where m is the number of samples in each series, and μ and σ are the mean and standard deviation of the series respectively. Both series have the same number of samples. In the table below, m is set to be 25000, which means 25 seconds of samples for each series. The correlation indexes calculated between any two series ranges from –1 to 1 with 1 being strongly positively correlated, -1 being strongly negatively correlated and 0 being no correlation. Six tests were performed and correlation results are summarized below. Table 4-1 shows the actual correlation values between a series and the delayed y series for the time instants where the system response

is around its maximum. Figure 4-5 illustrates graphically the correlation index changes between the *a* series and the y series as the time delay increases from 0 sec (no delay) to 0.25 sec. The rise and fall of the correlation index between the two series reflects exactly the actual rise and settling time of the system response *y* to input *a*.

Table 4-1: Correlation of delayed *y* and *r* series with the *a* series with the strongest correlation highlighted

***a*-series Test No.**	**Corrupted PPG – Correct PPG (y-series)**					
	No delay	+0.07s delay	+0.08s delay	+0.09s delay	+0.10s delay	+0.11s delay
1	0. 28	0. 86	0. 89	0. 89	0. 88	0. 86
2	0. 05	0. 90	0. 93	0. 92	0. 89	0. 83
3	0. 18	0. 92	0. 93	0. 92	0. 88	0. 81
4	−0. 30	0. 67	0. 74	0. 78	0. 79	0. 77
5	−0. 15	0. 72	0. 78	0. 81	0. 81	0. 79
6	0. 02	0. 74	0. 78	0. 81	0. 81	0. 79

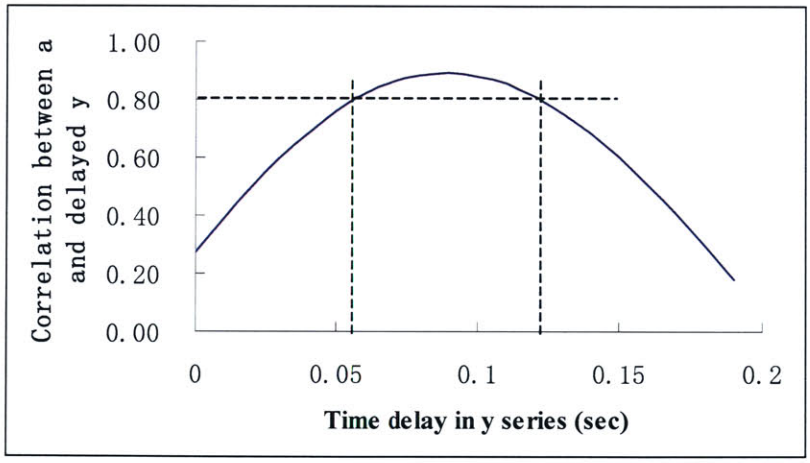

Figure 4-5: Plot of correlation index between a series and y series against the time delay in y series (Test 1 only)

From Table 4-1 and Figure 4-5, the following points can be observed and inferred

- The X-axis acceleration (*a* series) is strongly correlated with the PPG magnitude change due to X-axis motion (*y* series) for y series with time delay between 0.06 seconds and 0.12 seconds.

- The *a* series correlates best with *y* series with time delay around 0.08 seconds to 0.09 seconds. This means that the maximum effect of X-axis motion on PPG signal comes in 0.08 seconds after the motion is applied. With 1000 samples/sec sampling rate, this corresponds to 80 to 90 points delay from the current time instant, *t*, for the FIR model.
- It is valid to use the FIR model instead of the IIR model, as the response of the system to X-axis motion rises and decays quickly in around 0.2 sec. The response can be considered as finite.
- The linear FIR system model seems to be sufficient due to the high correlation index of around 0.9 between the *a* series and the delayed *y* series even without considerations of higher order terms.

Therefore, the FIR model in Equation (4-3) should be used. Moreover, the correlation analysis suggests a total system response time of around 0.2 sec, which corresponds to 200 discrete input points with 1000 samples/sec sampling rate. In view of this, it appears that the FIR model has to have a total of 200 coefficients (n=200). However, if considering the time duration where the correlation index is above 0.8, only the time duration of 0.06 seconds to 0.12 seconds after the motion is applied should be incorporated inside the FIR model. The issue of choosing the right value of n will be revisited in the later part of this chapter.

4.3 The Adaptive Noise Cancellation Algorithm

In order to determine the system parameters in Equation (4-3) and to remove the motion artifacts due to X-axis motion from the corrupted PPG signal to obtain the correct PPG, a suitable set of System Identification and noise-filtering techniques should be chosen. Before making the decision, let's first look at the System Block Diagram as well as the proposed Motion Artifact Cancellation Setup illustrated below.

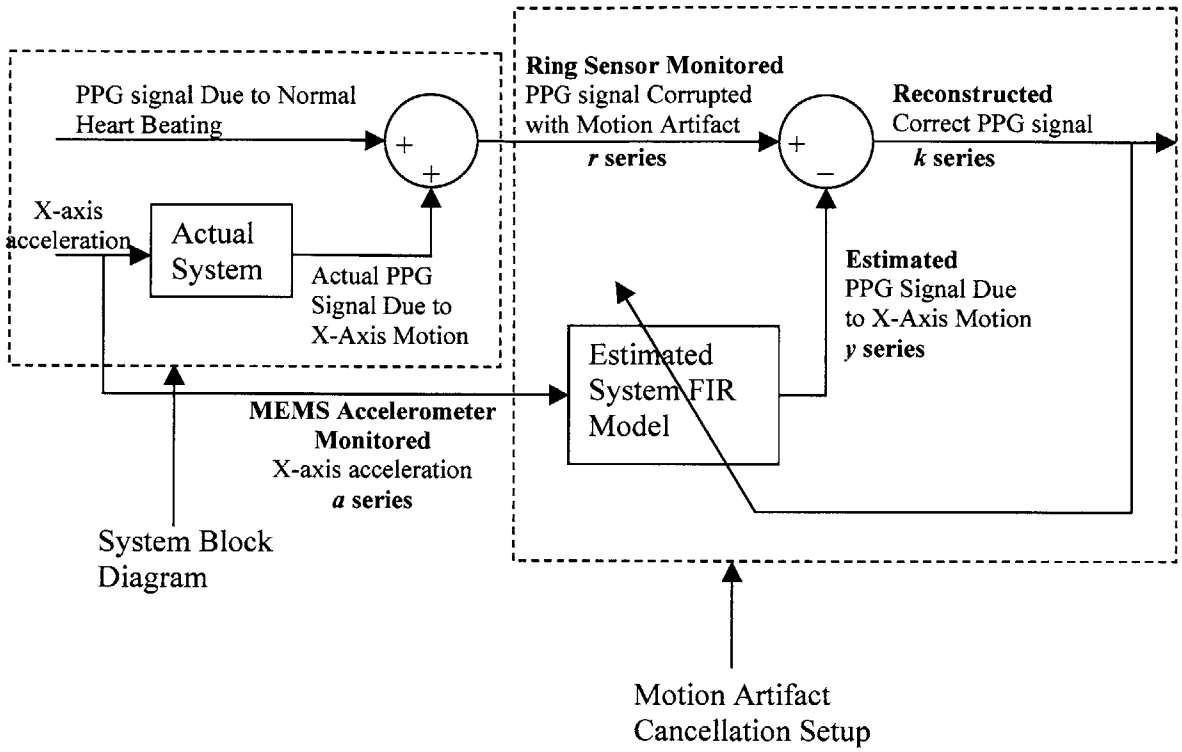

Figure 4-6: System block diagram showing the effect of X-axis motion on PPG signal as well as the proposed motion artifact cancellation setup

Looking at the System Block Diagram part of the figure, it can be seen that using the Ring Sensor, we will be able to obtain the PPG signal corrupted by the motion along X-axis. This corrupted PPG signal is the sum of the normal PPG signal due to heartbeat and the actual PPG signal due to X-axis motion. This is the PPG additive assumption that was made earlier on. Looking at the Motion Artifact Cancellation Setup part of the figure, it can be seen that with the measured Ring Sensor Signal (*r* series), the measured MEMS accelerometer signal (*a* series) and the knowledge of the estimated system FIR model, we can estimate the PPG signal due to X-axis Motion (*y* series), and also to estimate the correct PPG (*k* series). The system FIR model is not fixed due to the time-variant model for the blood flow inside the arteries. Therefore, the FIR model has to be tuned adaptively in real time. The estimated correct PPG (*k* series) should be used for tuning the model because of the exact resemblance between this setup and the setup for Adaptive Noise Cancellation algorithm.

Adaptive Noise Cancellation is an algorithm proposed by Bernard Widrow in his paper published in 1975 [14]. It is used for adaptive filtering of signals contaminated with noise sources, which can be separately measured. The setup is as follows.

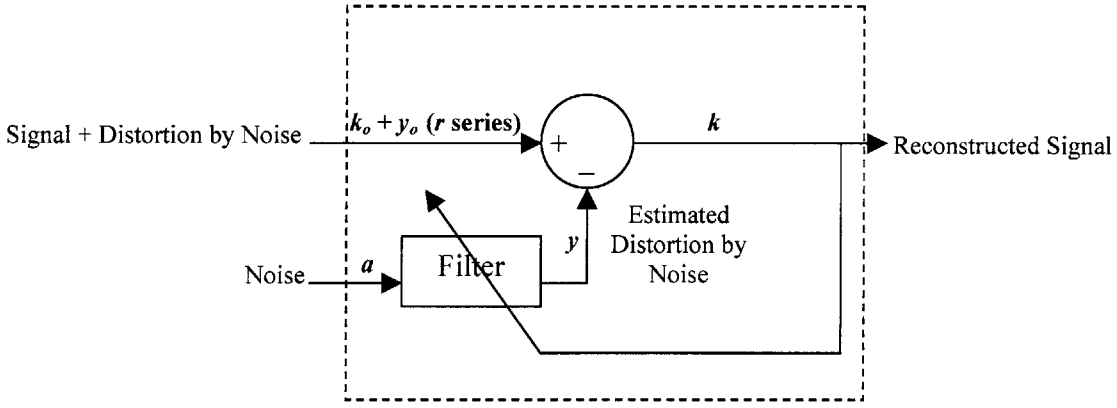

Figure 4-7: Graphic illustration of the Adaptive Noise Cancellation algorithm

This is exactly the same setup as the Motion Artifact Cancellation setup for the Ring Sensor PPG signal. Therefore, the X-axis acceleration can be viewed as the noise, and the correct PPG can be viewed as the signal that needs to be reconstructed. The adaptive filter for the Adaptive Noise Cancellation setup is usually an FIR model, and this further supports the choice of using FIR for the X-axis motion artifact modeling. The k_o+y_o is the r series used in the Ring Sensor model in Figure 4-6.

The Adaptive Noise Cancellation algorithm does not assume any prior knowledge of the adaptive filter (the FIR model), and it continuously adjusts the filter to minimize the error between y and y_o through minimizing the power in k. The following analysis explains the reason behind the algorithm.

$$E[k^2] = E[(r-y)^2] = E[(k_o + y_o - y)^2] = E[k_o^2] + E[2k_o y_o] - E[2k_o y] + E[(y_o - y)^2] \quad (4\text{-}6)$$

Since k_o represents the correct PPG due to heartbeat and y_o represents the PPG magnitude change due to X-axis motion, there should be near zero correlation between the two time series. Therefore, $E[2k_o y_o]$ and $E[2k_o y]$ can be neglected and Equation (4-6) becomes:

$$E[k^2] = E[k_o^2] + E[(y_o - y)^2] \quad (4\text{-}7)$$

Since $E[k_0^2]$ is the power of the correct PPG due to heartbeat and is fixed, to minimize $E[(y-y_o)^2]$ is the same as minimizing $E[k^2]$. This essentially means that the error between the estimated y and the actual y_o can be minimized if the power of the estimated output k is minimized. To perform this minimization, a simple Recursive Least Square (RLS) algorithm can be used for adaptively determining the coefficient of the FIR filter. The following is the setup for the RLS algorithm.

Based on Equation (4-3) and letting $\theta = [q_1, q_2 \cdots q_n]^T$ and $\varphi_t = [a_{t-1}, a_{t-2} \cdots a_{t-n}]^T$,

$$y = \theta^T \varphi_t \tag{4-8}$$

For the RLS algorithm, the following three calculations are performed in the sequence stated and recursively [14].

$$\begin{aligned} \theta_t &= \theta_{t-1} + \frac{P_{t-1}\varphi_t}{1 + \varphi_t P_{t-1} \varphi_t^T}(r_t - y_t) \\ P_t &= P_{t-1} - \frac{P_{t-1}\varphi_t \varphi_t^T P_{t-1}}{1 + \varphi_t P_{t-1} \varphi_t^T} \\ y_t &= \theta_t^T \varphi_{t+1} \end{aligned} \tag{4-9}$$

P is called the covariance matrix and the initial value P_0 is set to be an identity matrix of dimension n by n. θ_0 is set to be an n by 1 matrix of zeros. With the time sequence of y_t estimated using the above recursive algorithm, the reconstructed correct PPG is then equal to r_t-y_t.

In order for this algorithm to work well, one very important point needs to be noted. Within the time window of the FIR model (defined by the value of n), the expectations of the powers of the various series in Equation (4-6) and Equation (4-7) need to have consistent mean values throughout the whole time span of the test. This means that the two input signals (a series and r series) must have close-to-constant DC values. Shifting of the DC values will lead to shifts of the power expectations, which leads to inconsistent output from Equation (4-9). Since the corrupted ring sensor signal and the MEMS accelerometer readings are bound to have small DC shifts due to inconsistent sensor calibrations and electrical noises, the input signals to the Adaptive Noise Cancellation algorithm need to be treated first. For this application, I have chosen to use high-pass filtering to remove any unwanted DC noises that will cause shifting of mean values.

Before finalizing this section, let us revisit the issue of the determination of n for the algorithm and consider the following points:

- Due to the high sampling rate (1000 sample points per second) and the fact that the RLS algorithm needs to be performed for each new sample point, the computation is heavy and the size of the matrix becomes crucial. Since n determines the matrix dimension, even n=60 tends to be too large in consideration of the real time computation power that the computer can provide. For a simple calculation of $y = P_{t-1}\varphi_t$ alone, it will need (60+60) x 60 x 60 x 1000 = 432,000,000 algebraic computation for every single second. It will be far worse if n=200 is used. Therefore the smaller the n, the faster the computation. If the value of n can be reduced to 10, the amount of computation will be reduced by a factor of 216 to 2,000,000 computations per second.
- Also, considering the time variant nature of the system due to unpredictable motion, when the external X-axis acceleration applied has a high frequency, the system model parameters change quickly. Therefore choosing a short time window for the FIR (smaller value of n) will make the model adapt quicker to the frequent system changes and will improve the transient response. Figure 4-8 on the next page compares differences in choosing n=10 and n=60 to illustrate this point.

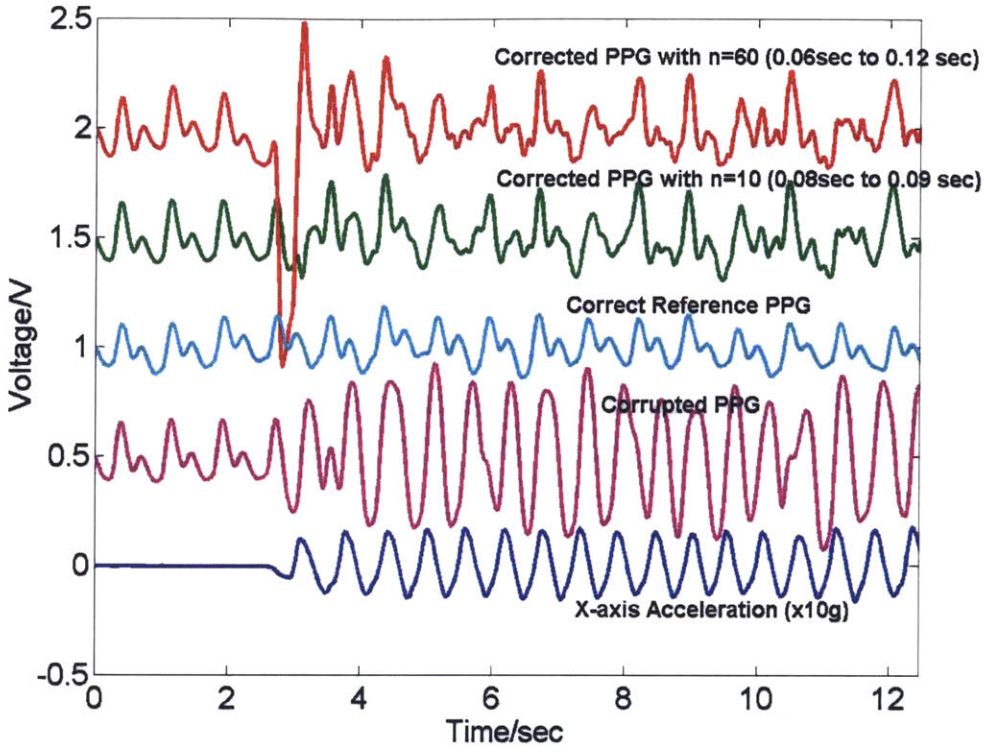

Figure 4-8: Comparing the corrected PPG with n=60 and n=10

It is obvious from the above figures that n=10 is better than n=60 in terms of transient response from no motion to X-axis acceleration. Since n=60 does not show any other advantage over n=10, n=10 should be adopted since it helps to save computation time.

4.4 Experimental Results

As analyzed in the previous section, the peaking of the effect of X-axis motion on PPG signal occurs at 0.08s after the motion is applied. This is equivalent to 80 data points for the 1000 samples/sec sampling rate. Therefore, the 10 input points have to be chosen around the 80th data point before the current time t and the φ vector is adjusted to become

$$\varphi_t = [a_{t-80}, a_{t-81} \cdots a_{t-80-n+1}]^T \tag{4-10}$$

where n=10. The rest of the algorithm remains unchanged and the dimension of the covariance matrix P becomes 10 by 10 instead.

The following figures show the reconstructed PPG signals from the X-axis motion corrupted PPG signals measured by the Ring Sensor on the moving left hand. The actual correct PPG signals were measured on the stationary right hand and were displayed together for comparison. The two sensor inputs for the Adaptive Noise Cancellation algorithm (the corrupted PPG signal and the X-axis acceleration) are included on the same figures as well. The magnitudes of the three PPG data series have been linearly shifted for charity of representation. The magnitude of the X-axis acceleration data is not shifted but scaled about the time-axis by a factor of 0.1. This means that the voltage-axis shows 0.1 times the actual X-axis acceleration measured in G ($10 m/s^2$). Vertical lines are drawn to compare the systolic peaks of the reconstructed PPG signal and those of the actual correct PPG.

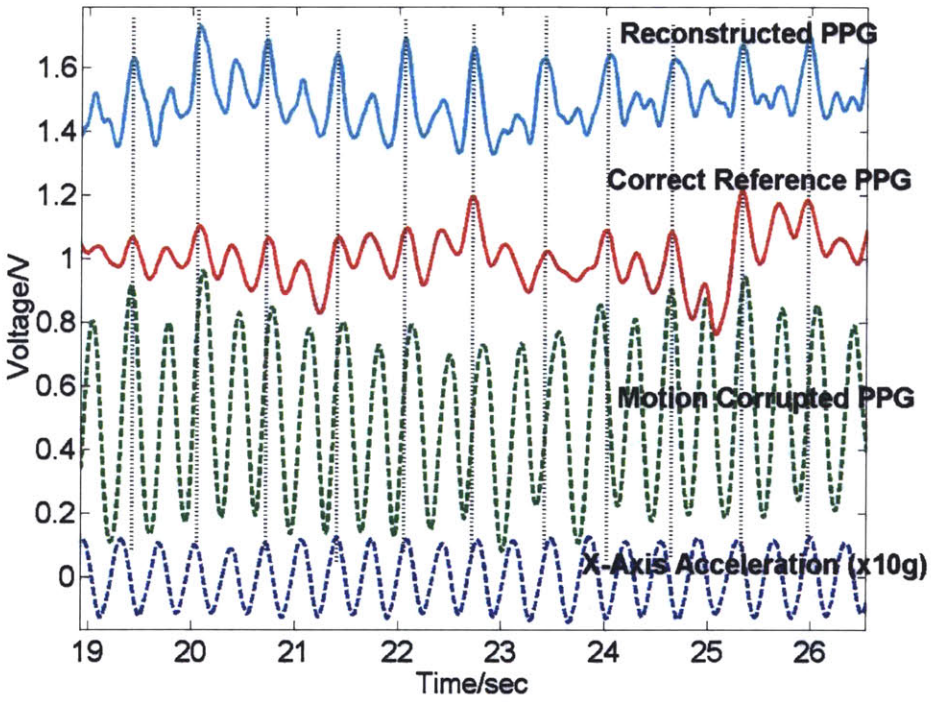

Figure 4-9: Comparing the reconstructed PPG with the correct reference PPG (1 of 3)

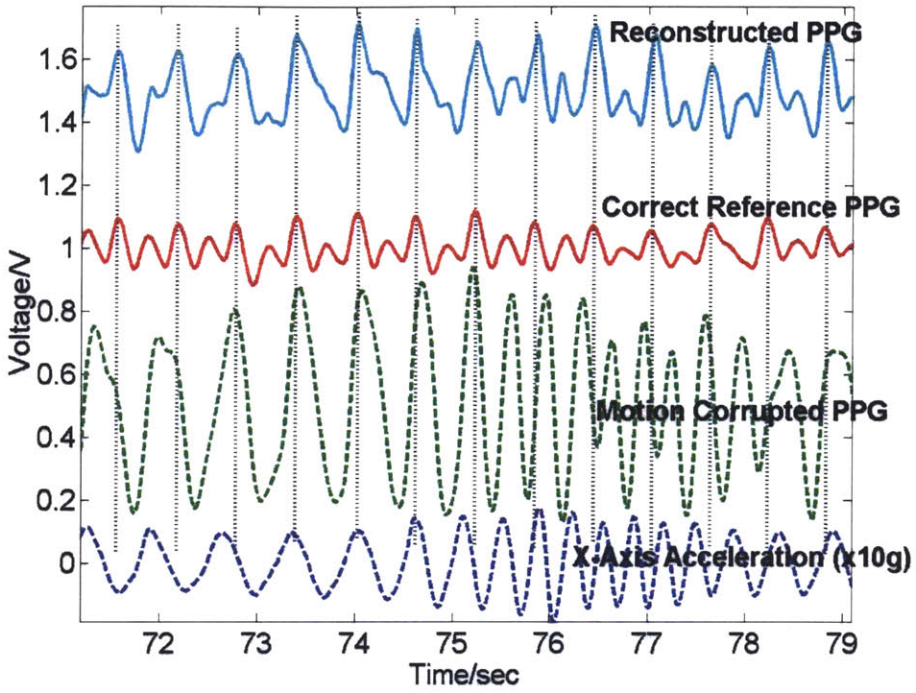

Figure 4-10: Comparing the reconstructed PPG with the correct reference PPG (2 of 3)

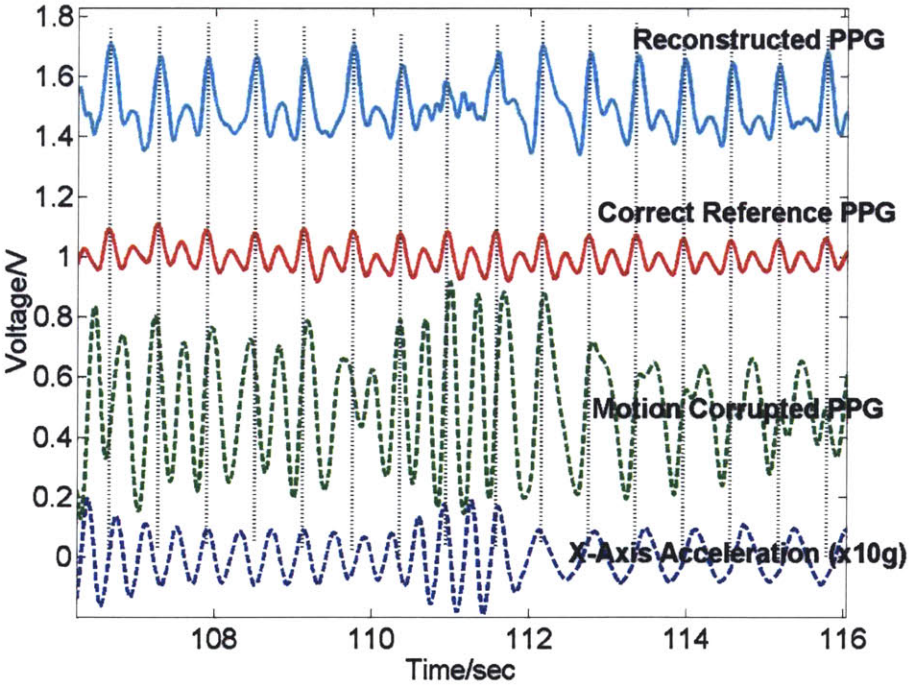

Figure 4-11: Comparing the reconstructed PPG with the correct reference PPG (3 of 3)

From the above three figures, it can be seen that the Adaptive Noise Cancellation algorithm is very successful. Not only do the peaks get reconstructed for almost 100% of the time, but the correct shapes of the waveform are recovered most of the time as well.

Looking at a commercial PPG device (produced by Heart Math Group) that is built for analyzing HRV further contrasts the higher capability and reliability of the Ring Sensor with its ability in rejecting motion artifacts in all three possible motion axis. See Figure 4-12 for details.

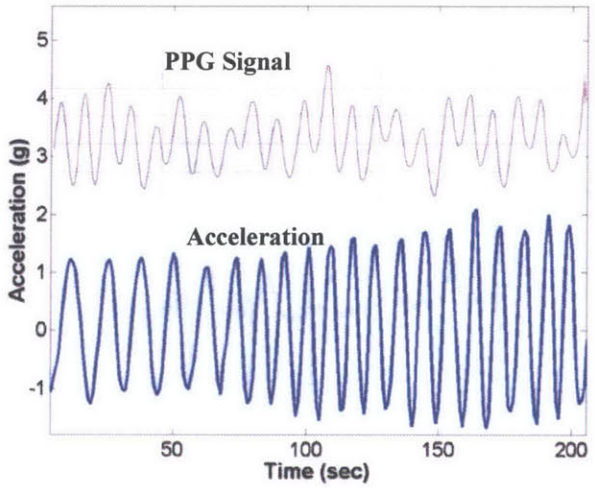

Figure 4-12: PPG waveform from a PPG sensor recently marketed by Heart Math group for detecting HRV. The PPG waveform is totally distorted at around 1G of acceleration.

5 RING SENSOR APPLICATION FOR DRIVER MONITORING ON THE ROAD

With all the development of the Ring Sensor discussed in the previous two chapters, let's look at its application on driver monitoring (chapter 2) and some practical problems that need to be solved.

5.1 Determining Beat-to-Beat HR

Beat-to-beat HR (or other equivalent forms such as RR-interval) is the basis for all the existing HRV analysis [14]. Conventionally, beat-to-beat HR is estimated based on the RR-interval of the ECG signal shown in Figure 5-1 below.

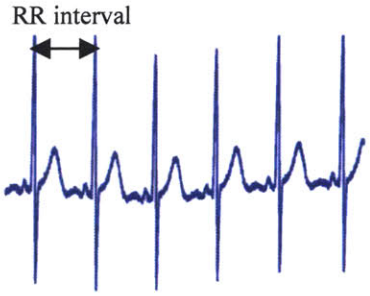

Figure 5-1: Typical ECG signal

Due to the sharp peak corresponding to each cardiovascular systolic point, it is easy to determine the peak-to-peak distances and thus the beat-to-beat HR. However in the case of PPG signal as can be seen below in Figure 5-2, the systolic peaks are less sharp compared with the rest of the pulse wave and there is also a second peak existing for normal healthy person.

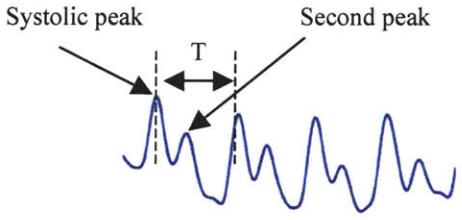

Figure 5-2: Typical PPG signal

Nevertheless, the time intervals T between successive systolic peaks in the PPG signals are almost equivalent to the RR intervals in the ECG signals. Figure 5-3 compares the beat-to-beat HR calculated using the PPG signals with that calculated by the ECG signal. Figure 5-4 compares the HRV calculated using the beat-to-beat HR obtained with both the PPG and the ECG signals. For reference purpose, a gold standard PPG measurement device (Nellcor sensor) is included as well.

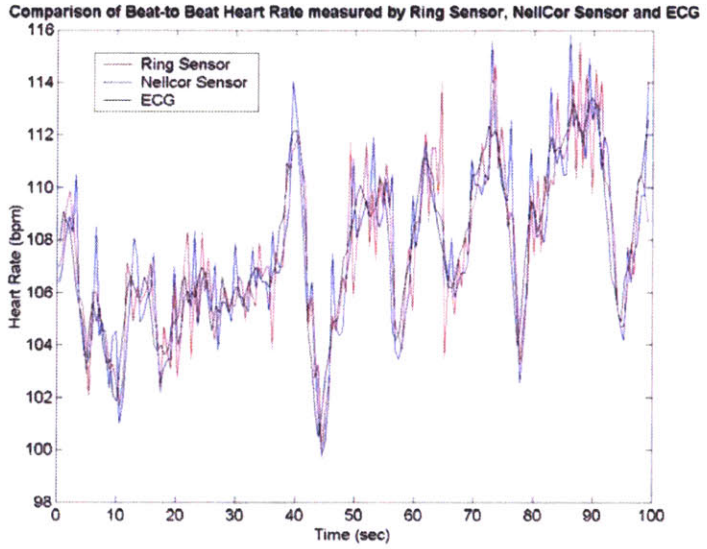

Figure 5-3: Beat-to-beat HR compared between ECG, Ring Sensor and Nellcor Sensor

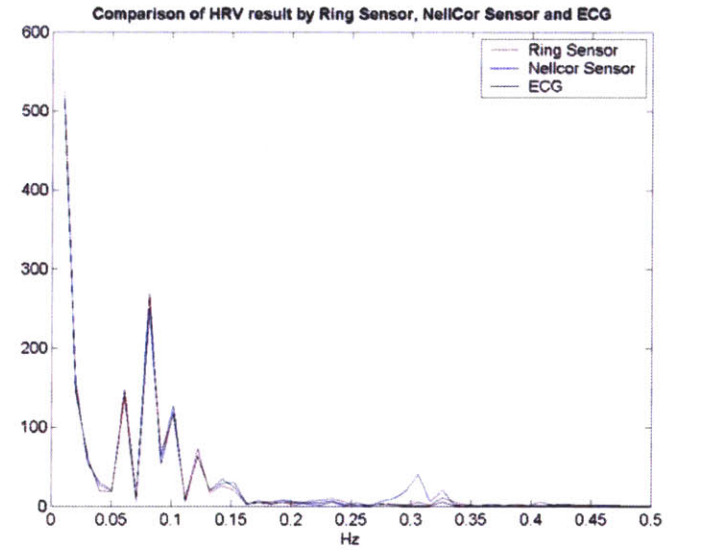

Figure 5-4: HRV calculated from the beat-to-beat HR measured by ECG, Ring Sensor and Nellcor Sensor

These two figures show that the PPG signals obtained from the Ring Sensor are capable of measuring the beat-to-beat HR and HRV, and the measurement result is very close to that obtained using the standard ECG device.

Despite the feasibility of using PPG signal for beat-to-beat HR measurement, the requirement for a clean and non-distorted PPG waveform is still essential, as any missing systolic peaks will lead to missing HR readings. When it is out on the road, the harsh road conditions (high accelerations at bumps and sharp turns) are still able to distort the Ring Sensor's PPG signals occasionally despite all the motion-artifact designs that have been implemented. This leads to occasional missing beat-to-beat HR data. On the other hand, direct sunlight can cause signal saturation due to the relatively low intensity of the LED. These two problems have to be addressed before the HRV analysis can be performed using the beat-to-beat HR data.

5.2 Preventing Signal Saturation under Direct Sunlight Influence

As discussed in the original work on the Ring Sensor [13], the sensor works on the principle of varying light absorption due to the changing blood volume inside the blood vessel brought about by the pressure wave sent down by the heart beating. The Ring Sensor has a photodiode and an LED that does the detection of the changing light absorption by the blood. Therefore, the LED is the light source that the rest of the Ring Sensor circuit is based on for signal filtering, amplification and tuning. The LED that has been chosen for the Ring Sensor is a strong local light source (30 mcd luminous intensity at 660nm wavelength) for its size. When it is used in most indoor environments as well as outdoors with no direct sunlight, the light source provided by the LED is dominant and the subsequent circuit design is valid. However, whenever there is direct sunlight shining on the sensor band, its luminous intensity largely surpasses that of the LED and causes both the base DC level and the AC amplitude of the light saturation in the finger to increase considerably. This makes the original LED-oriented sensor design invalid, as the same amount of AC-amplification and DC reference level designed for the light source provided by the LED will saturate the sensor output signal to its maximum (which equals to the DC power supply voltage to the sensor) under direct sunlight. This essentially means that there will be no usable PPG signal for that duration of direct sunlight exposure. The following figure shows one

section of the road test data that has been saturated by the direct sunlight and has become unusable for HR estimation.

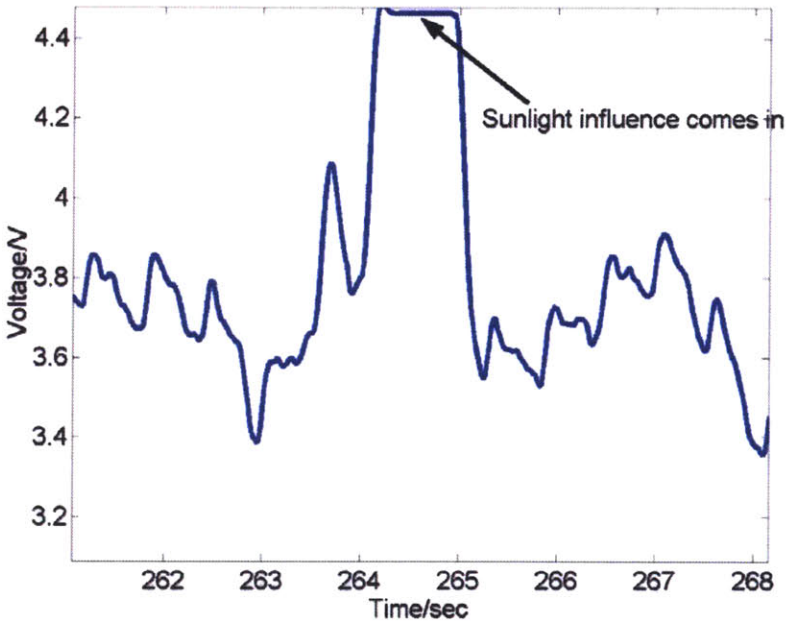

Figure 5-5: Ring Sensor's PPG wave saturated by sunlight

In order to solve this problem, the level of AC amplification as well as the DC-reference in the circuit has to be automatically adaptive to the real-time lighting condition at the point on the finger where the sensor head is attached. Due to the power consumption consideration, complicated adaptive amplification circuitry is not suitable for the onboard electronics on the Ring Sensor. Therefore, the amplification level is fixed at the maximum that will still keep the signal from saturation under direct sunlight. With the AC-amplification fixed, the DC-level is designed to adjust by itself to provide the correct reference point for amplification. For example, when there is sunlight, the DC-level of the signal is usually at 0.2V and the DC reference for the AC-amplification has to be set to 0.2V; when there is sunlight, the DC-level of the signal will shoot up to 2-3V and the DC reference has to be set automatically to follow that. Furthermore, due to the high sensitivity of light intensity to sensor locations, the local light intensity information at the sensor head is needed to provide the correct DC reference. Therefore, the DC reference information has to be obtained from the actual raw PPG signal (pre-amplified signal) instead of any reference points elsewhere on the finger. In fact, experimental results have shown

that placing a DC light reference anywhere else makes the sensor setup unusable, even if it is just millimeters away.

The automatic DC reference setting is done using the following dynamic averaging circuit.

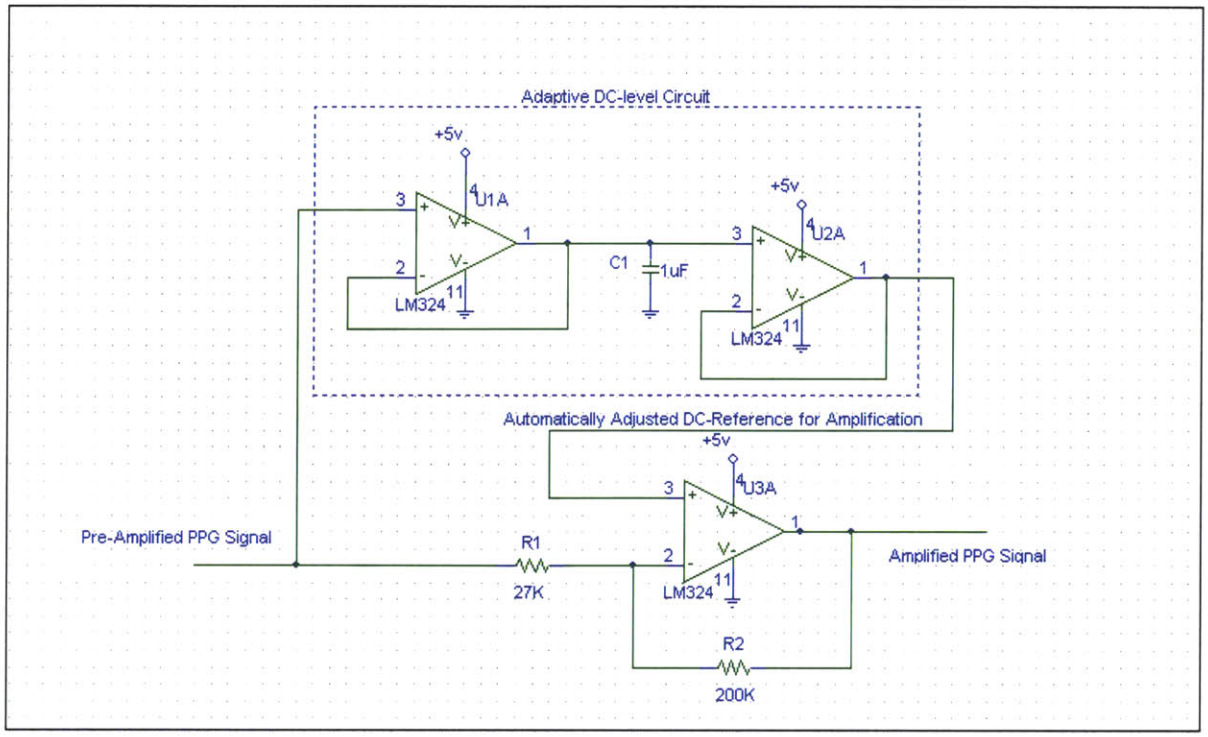

Figure 5-6: Automatic DC Reference Level Setting and Amplification Circuit

For the complete new Ring Sensor circuit, please refer to the Appendix. With this improvement, the sunlight saturation problem is fixed. Figure 5-7 shows the PPG signals obtained from six human subjects, both male and female, ranging in age from 24 to 30. The experiment is done under simulated direct sunlight environment using a strong flash light right above the sensor band. None of the PPG signals are saturated under the strong ambient light. Therefore, the sunlight saturation problem is solved.

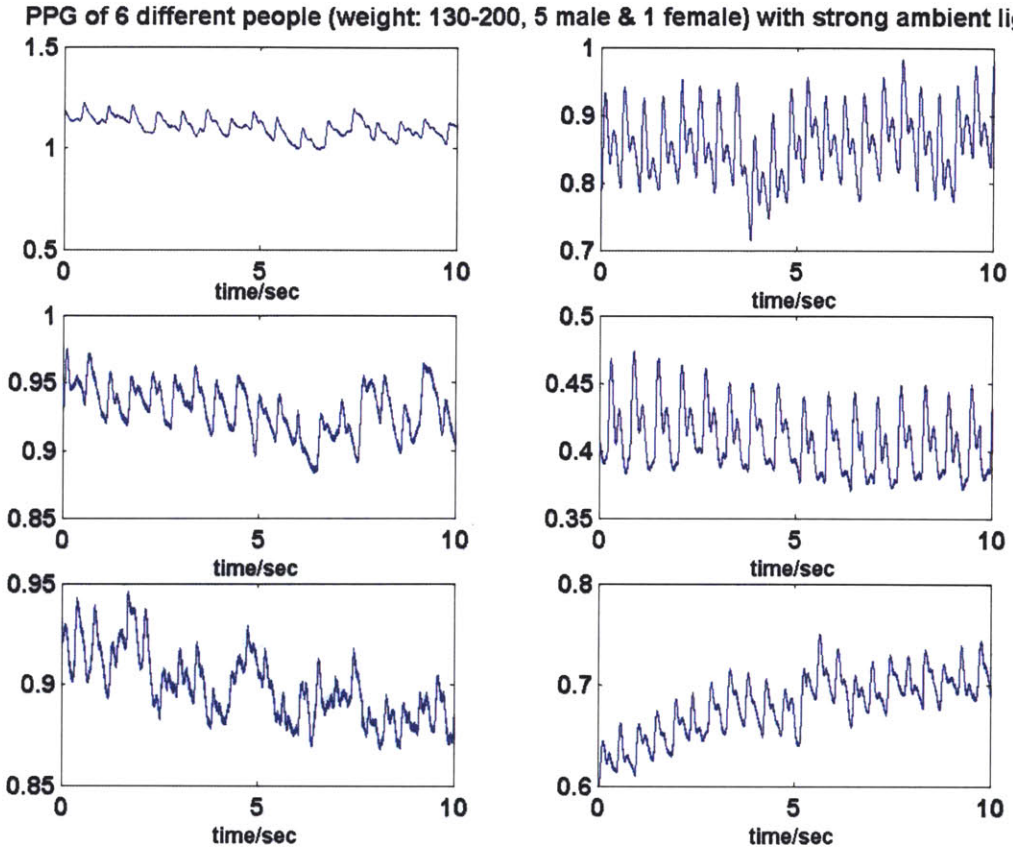

Figure 5-7: PPG signal from 6 different people with strong ambient light

5.3 Discrete Fourier Transform of Beat-to-Beat HR Having Missing Points

Before addressing the problem of missing HR data points, let's take a preliminary look at some road test results and see how badly the PPG signal gets distorted.

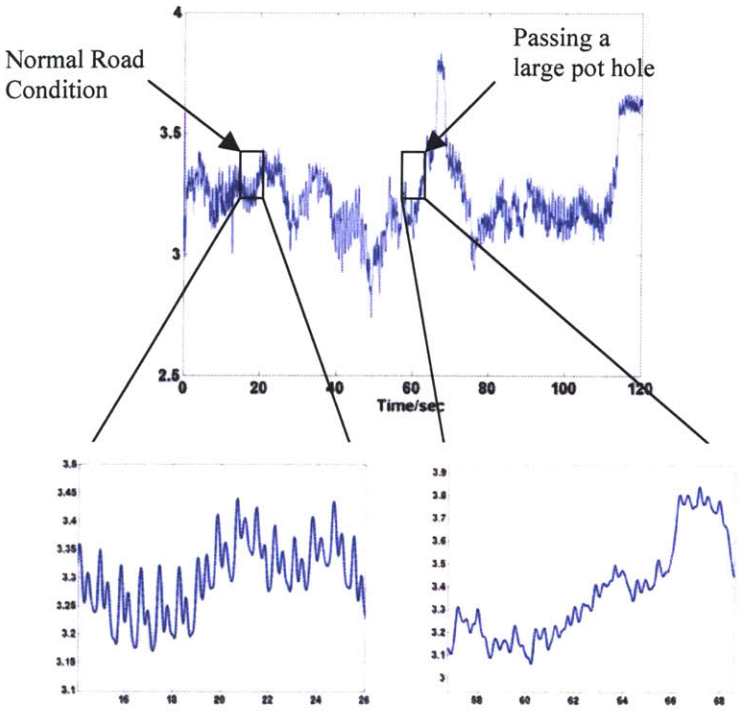

Figure 5-8: PPG waveform from part of the road test with two sessions enlarged

From the above result, it can be seen that the PPG waveform of the Ring Sensor is clean for normal road conditions but becomes distorted when the road surface condition is rough. Therefore, it is reasonable to expect that the new Ring Sensor will work well for normal road conditions and will miss some pulses when the driver passes large potholes or makes sharp turns. In the later two cases, the acceleration that the driver experiences is believed to be more than the 30 m/s^2 produced in the control lab environment for Ring Sensor testing.

In order to have a valid frequency domain analysis on HRV, at least five continuous minutes of valid beat-to-beat HR result are needed [15]. Since the road test result suggests the possibility of missing beat-to-beat HR reading due to distorted PPG pulse wave over rough road surfaces, some data processing algorithms are needed to recover those missing points. This section discusses the details of finding beat-to-beat HR and the algorithms for missing data recovery.

5.3.1 The Problem

The standard procedure for obtaining HRV is to compute the Fourier Transform of the entire time series of beat-to-beat HR. Let *h(i)* be a time series beat-to-beat HR and N be the total number of samples, hence $1 \le i \le N$. The Discrete Fourier Transform of *h(i)* for the finite time interval, $1 \le i \le N$, is given by

$$g_k = \frac{1}{N}\sum_{i=0}^{N-1} h(i)\exp(-j\frac{2\pi ki}{N}), \qquad k = 0,1,\cdots, N-1 \tag{5-1}$$

where $k = 0,\cdots, N-1$ is the frequency index, and corresponds to the actual frequency ω_k by $\omega_k = 2\pi T_s \frac{k+1}{N}$, where T_s is sampling period.

In this application on HRV, the frequency components we would like to identify are at very low frequencies, *0.01 Hz ~ 0.5 Hz.* This implies that data must be obtained for a long period of time. To cover one complete cycle of low frequency sine waves, *0.01 Hz,* for example, data must be taken for *100 seconds.* In fact, the standard time duration for HRV analysis is at least five minutes [15]. Furthermore, such data must be taken continually without interruption. This turns out to be unrealistic, since PPG signals may be corrupted with disturbances and often HR data cannot be obtained for certain periods. Although the Ring Sensor is able to reject most of the motion artifacts, as described previously, it is still infeasible to take data uninterruptedly for such a long period of time due to unforeseen extreme road conditions.

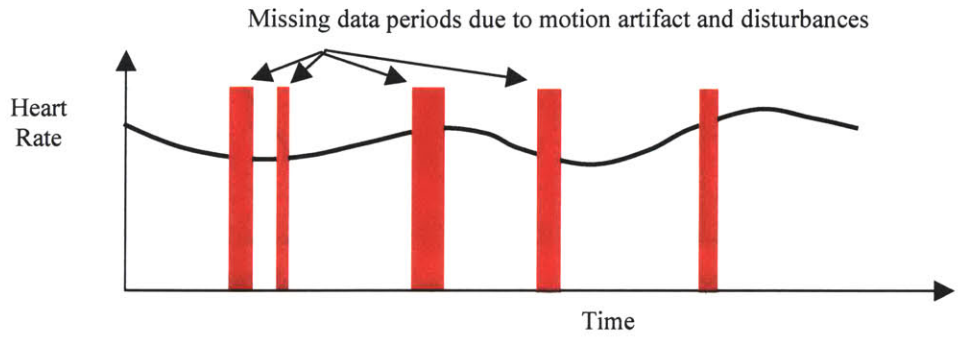

Figure 5-9: Data with corrupted periods

Figure 5-9 illustrates a HR time series with occasional corrupted periods. The frequent occurrence of missing data makes the uninterrupted period not long enough to recover the low frequency components in HRV frequency spectrum. Therefore we must use the entire duration of data, although it includes missing data periods.

There are some ad hoc methods to resolve this difficulty. For example, one may simply ignore the missing data periods and append the segmented data durations into one continuous time series, as shown in Figure 5-10(b). This distorts the phase information of each frequency component and results in an inconsistent power spectrum. Another two similar ad hoc methods are to reconstruct the missing data using the Linear Curve Fitting method (Figure 5-10(c)) or to replace missing data by the mean of the valid data points (Figure 5-10(d)). Both methods will cause higher frequency components to be missed as the missing period prolongs. However since we are interested in only the low frequencies (<0.5Hz), missing periods of less than 2 seconds will still be tolerable.

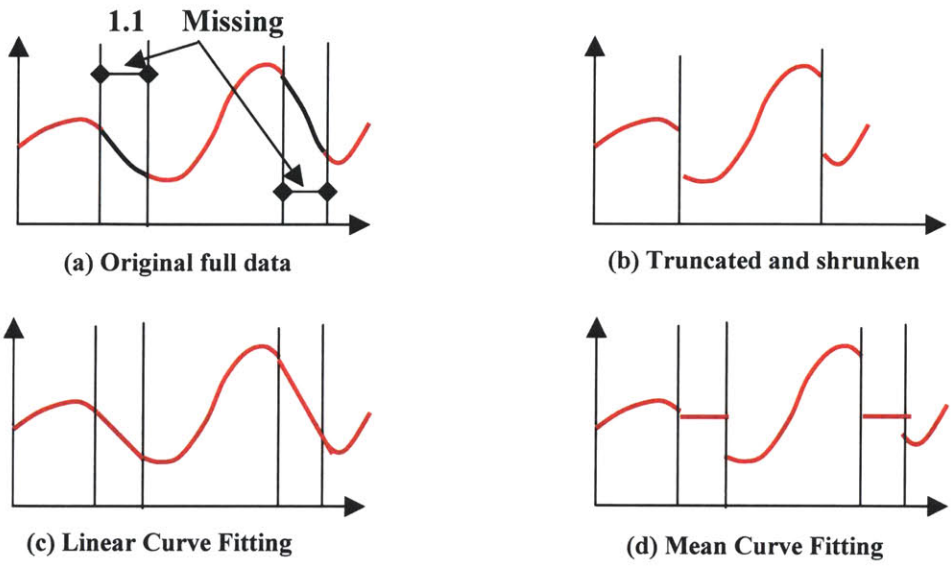

Figure 5-10: Ad hoc methods for dealing with missing data points

Since the validity of these ad hoc remedies are questionable, a systematic method for estimating the HRV power spectrum from incomplete data set having missing data periods will be developed in the following section. To this end we examine the computational structure of the Discrete Fourier Transform given by Equation (5-1). The Fourier Transform g_k provides the strength of periodicity in the original time series with respect to the k–th frequency component. A set of original data points at the same phase angle of the k–th frequency component are averaged and multiplied with the exponential function. When some data points are missing, this averaging may cause some error, providing unfaithful results.

5.3.2 New DFT Algorithm

Let T_s be the sampling interval with which data are taken; $h(t) = h(T_s I)$, or $h(i)$ for simplicity, $1 \le i \le N$. Substituting this to Equation (5-1) yields DFT of the HR time sequence,

$$G(-j\omega) \cong \frac{1}{N}\sum_{i=0}^{N-1} h(i)\exp(-j\omega T_s i), \qquad (5\text{-}2)$$

In discrete form, DFT is computed at discrete frequencies, ω_k, usually spaced equally in frequency;

$$\omega_k = \frac{2\pi}{T_s N} k, \qquad k = 0,1,\cdots, N-1 \tag{5-3}$$

In the new DFT algorithm, DFT is computed at discrete frequencies but with different frequency spacing

$$\omega_p = \frac{2\pi}{pT_s}, \qquad p = 2,3,\cdots, P \tag{5-4}$$

Unlike the standard DFT algorithm, the frequency spacing of this DFT decreases as the frequency becomes smaller. This is a desirable feature for computing HRV, since very low frequencies, less than 0.01 Hz, must be computed more finely than high frequencies, say larger than 0.1 Hz. The new varying frequency spacing gives finer discretization as the frequency decreases. The fastest frequency, on the other hand, is bounded by *p=2,* according to the Sampling Theorem. The slowest frequency is bounded by the duration of data, or the total number of data points, $p \le P = \left[\frac{2\pi}{NT_s}\right]$, where [x] represents the largest integer not exceeding x.

For this particular frequency spacing, DFT coefficients can be computed despite missing data periods. Basically Fourier Transform provides the strength of periodicity imbedded in the original time series data by evaluating the correlation between the time series data and trigonometric (exponential) functions with various frequencies. For each frequency ω_p, every cycle of the trigonometric function corresponds to p sample points. According to Equation (5-4), the period given by $pT_p = 2\pi/\omega_p$. Therefore every cycle contains an integer number of sample points, *p.* See Figure 5-11. If data point *I* is the $\ell - th$ data point in the *(m-1)-st* period, it can be written as:

$$i = m \cdot p + \ell, \qquad \ell = 0,1,\cdots, p-1, \quad m = 0,1,\cdots, M-1 \tag{5-5}$$

where *M* is the number of cycles involved in the observation time span over which DFT coefficients are computed.

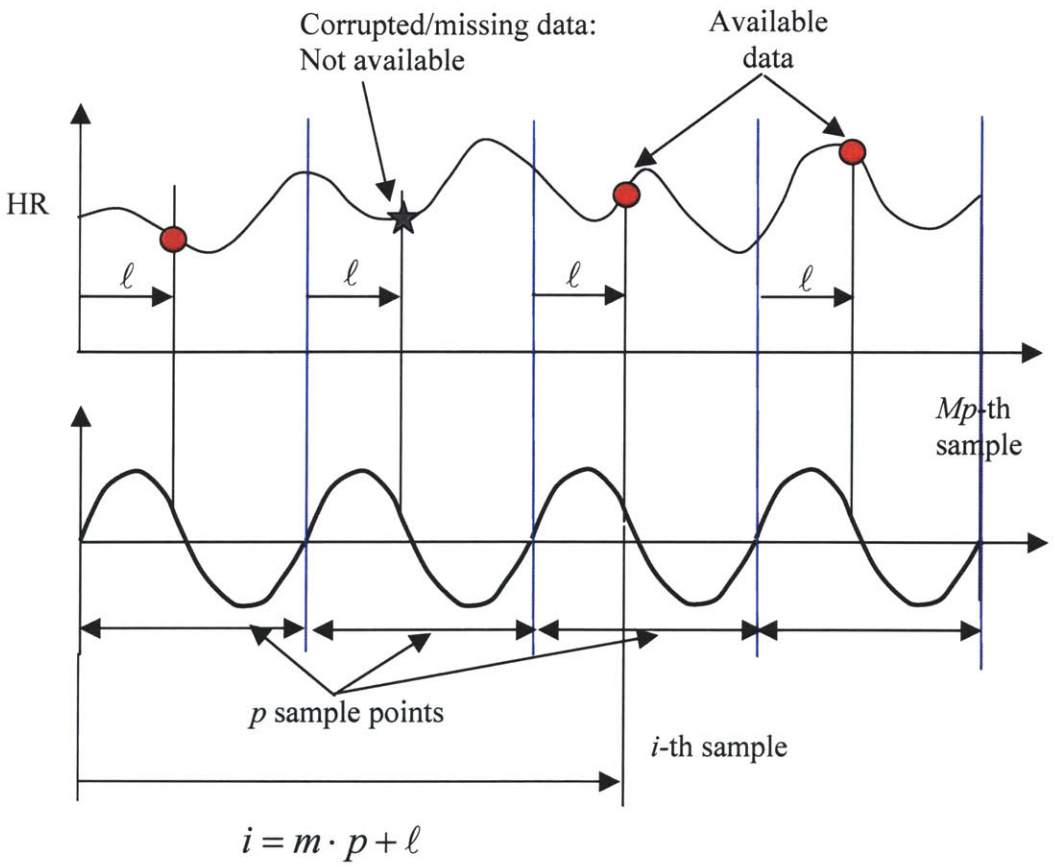

Figure 5-11: Graphical illustration of the new DFT algorithm for recovering missing data points

The observation time span is an important design parameter in particular for identifying low frequency HRV. It is interesting to note that high frequency variation may be determined in a shorter time span, while low frequency variation may need a longer time span. Physiological aspects should also be considered in determining the time span for each frequency range, as will be discussed later. For now, let's consider M complete cycles of observation time span for identifying the periodicity of frequency ω_p in the HR data. The DFT coefficient of frequency ω_p for M complete cycles of HR data is then obtained by substituting Equations (5-4) and (5-5) into Equation (5-2) and setting $N=pM$;

$$
\begin{aligned}
G^*(j\omega_p) &= \frac{1}{pM}\sum_{m=0}^{M-1}\sum_{l=0}^{p-1} h(p\cdot m+l)\exp(-j\frac{2\pi}{p}(p\cdot m+l)) \\
&= \frac{1}{pM}\sum_{m=0}^{M-1}\sum_{l=0}^{p-1} h(p\cdot m+l)\exp(-j2\pi m)\exp(-j\frac{2\pi l}{p}) \\
&= \frac{1}{pM}\sum_{\ell=0}^{p-1}\exp(-j\frac{2\pi \ell}{p})\sum_{m=0}^{M-1} h(p\cdot m+\ell) \\
&= \frac{1}{p}\sum_{\ell=0}^{p-1}\exp(-j\frac{2\pi \ell}{p})\bar{h}(l;p)
\end{aligned}
\tag{5-6}
$$

where $\bar{h}(l;p)$ is the average of the l-th data points over the M cycles of data, as shown in Figure 5-11.

$$
\bar{h}(l;p) = \frac{1}{M}\sum_{m=0}^{M-1} h(p\cdot m+l) \tag{5-7}
$$

It should be noted that the summation over m can be computed prior to the multiplication with the exponential function in the last expression of Equation (5-6). Therefore the number of multiplications reduces, compared with that of the first expression.

The final expression of Equation (5-6) is not only computationally efficient but also quite powerful for dealing with a time series having missing data periods. When all the data points are available, the above averaging is literally performed. However, once some data are missing, it cannot be computed in its original form. The missing data must be filled and the optimal value of those missing data is given by the average of the other available data. Without loss of generality let us assume that, among the M data points, only the first M^* points are available, i.e. the last M-M^* points are missing, then the average is given by

$$
\hat{h}(l;p) = \frac{1}{M^*}\sum_{m=0}^{M^*-1} h(p\cdot m+l) \tag{5-8}
$$

It can be shown under mild assumptions that the expected estimation error is minimum when the missing data are filled with the above average of the available data. Using Equation (5-8) in Equation (5-6) yields the estimated DFT coefficient $\hat{g}_p$,

$$
\hat{g}_p = \frac{1}{p}\sum_{l=0}^{p-1}\exp(-j\frac{2\pi l}{p})\cdot\hat{h}(l;p) \tag{5-9}
$$

for frequency $\omega_p = 2\pi / pT_s$.

5.3.3 Remarks

In the above method, the coefficients $\hat{g}_p$ do not have to be computed for all the discrete frequencies. Unlike the standard FFT, coefficients of specific frequencies relevant to HRV can be computed separately. This reduces computational complexity. Since the frequency of HR is approximately *0.5 Hz,* the sampling period is around *0.5 sec.* Therefore the fastest frequency component is $\omega_p = 1\ Hz$, for p=*2*, and the next frequency is *0.67 Hz,* for p=*3*, both of which are irrelevant to HRV, hence omitted. For p=*4, 5, 6, 7, 8,* ω_p = *0.5, 0.4, 0.333, 0.286, 0.25 Hz,* respectively. This is the range of respiration rate and is overlapped with the high frequency HRV range, so care must be taken to differentiate the two. All the frequency components should be computed. The vicinity of $\omega_p = 0.1\ Hz$, is an important range strongly connected to the parasympathetic activities. Therefore the Fourier coefficients should be computed densely around p=*20.* Similarly, low and very low frequency ranges should be computed at the right granularity level to meet both accuracy and computational efficiency. This can be accomplished by selecting a set of integers p having appropriate intervals. Note that the frequency separation becomes smaller as the frequency gets lower according to Equation (5-4).

One of the features of the proposed method is that the data are averaged for each p prior to the multiplication with the exponential function. This separation reduces computational complexity as mentioned before. Furthermore, this separation would allow us to streamline the storage and computation of time-series data for real-time applications. Although this part of research remains unfinished and needs continued investigation, the outline of the real-time algorithm is summarized below.

In real-time applications, time-series data must be processed while acquiring data, rather than batch processing a large block of data. To this end we divide the incoming data into small segments of data, and update the Fourier coefficients $\hat{g}_p$ every time a new block of data is processed. The computation of average $\hat{h}(l;p) = \frac{1}{M^*}\sum_{m=0}^{M^*-1} h(p \cdot m + l)$ can easily be extended to a recursive form. Given a new block of data, the average can be updated by taking a weighted average with the new data. See Figure 5-12. Furthermore, we can introduce a forgetting factor

α, $(0 < \alpha < 1)$ to more heavily weigh the recent data and to suppress the contribution from old data. Since the physiological system under consideration is a time-varying system, we would like to identify recent trends of HRV rather than its history. However, data must be observed for a time span that is long enough to estimate periodicity at low frequencies. This implies that a recent data block must be weighted more, but it must be augmented with some older data blocks as well. As the data block becomes older, its weight should be lowered and finally vanish. This can be implemented simply by multiplying a forgetting factor to the previous result, i.e. the average $\hat{h}(l;p)$.

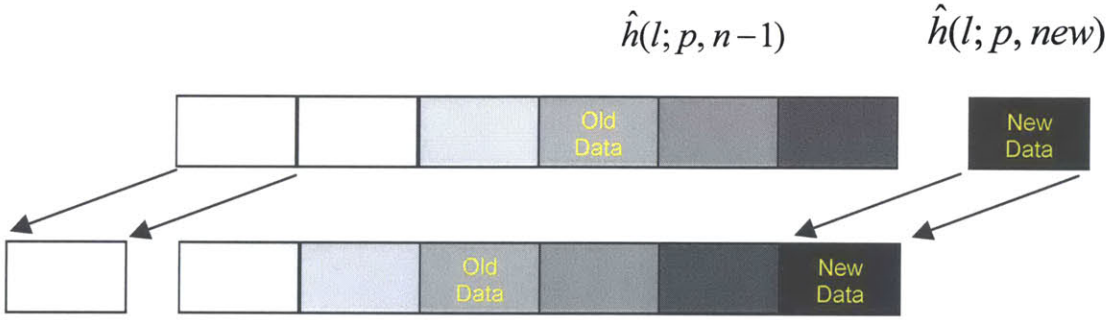

$$\hat{h}(l;p,n) = \hat{h}(\ell;p,new) + \alpha \cdot \hat{h}(\ell;p,n-1)$$

Figure 5-12: Recursive formulas and forgetting factor

Care must be taken in selecting this forgetting factor. Physiological aspects must be taken into account, since the rate of changes in HRV is dependent upon the dynamic response of the sympathetic and parasympathetic systems. Sympathetic and parasympathetic tones are altered with specific time constants. The forgetting factor must be selected in such a way that is consistent with these physiological activities. The time constant associated with the sympathetic tone is different from that of the parasympathetic tone. Fatigue may occur much slowly; hence its time constant will be very slow. Note that each physiological behavior is connected to a specific range of frequencies. Therefore, the forgetting factor should be given for each frequency range. Fortunately, the proposed computational algorithm allows us to implement multiple forgetting factors without difficulties. Since the average is computed separately for each frequency, a different forgetting factor can be used for each frequency range.

There are numerous challenging issues worth further investigation. The new DFT algorithm has the potential to be a powerful method for real-time computation of HRV for driver monitoring.

5.3.4 Algorithm Comparison

In order to compare the ability of the different algorithms in recovering missing data points for frequency spectrum analysis, a simulated 20 minutes of beat-to-beat HR data were used. The simulation data is a sum of seven different frequency components (0.01Hz, 0.03Hz, 0.05Hz, 0.1Hz, 0.15Hz, 0.3Hz and 0.5Hz). The mean HR is set to 80 beats/min and the range of variation is set to be ±10 beats/min. The absolute energy for each frequency component is randomly determined by uniform random distribution. This is a typical beat-to-beat HR pattern of a normal healthy adult [15]. Figure 5-13 below shows the simulated HR in time domain and the frequency domain HRV analysis.

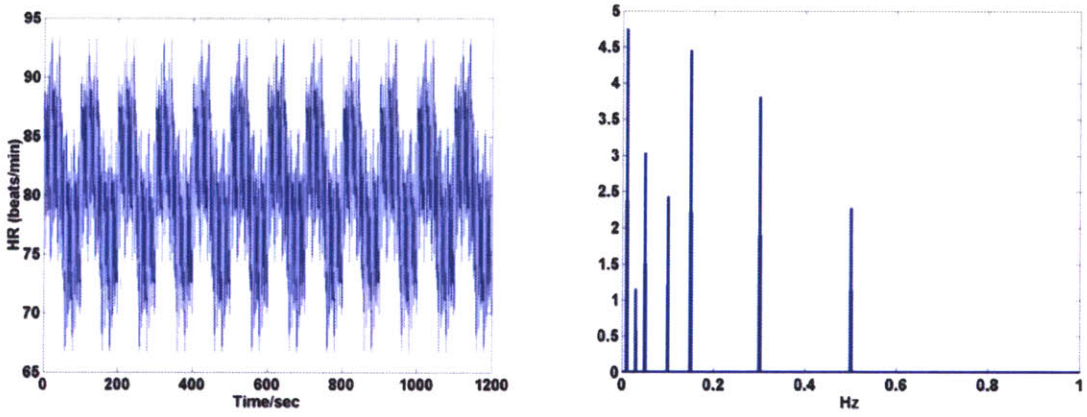

Figure 5-13: Time sequence data on the left and the frequency analysis on the right. The seven frequency components can be seen clearly from the frequency spectrum analysis.

10% of the simulated HR data points are randomly taken out to simulate the missing HR data occurring on the road and the four different algorithms discussed earlier (a. Time domain truncation, b. Linear curve fitting, c. Mean curve fitting and d. New DFT algorithm based on stochastic averaging) are applied to the same corrupted data set and the frequency analysis results are compared in Fig 5-14 below.

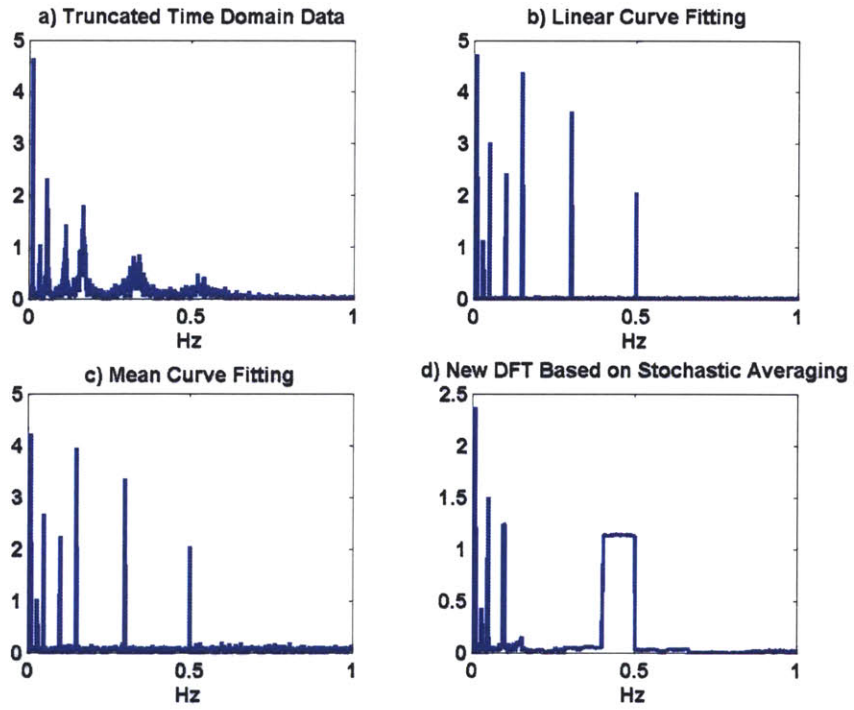

Figure 5-14: The comparison of the frequency spectrum analysis using the four different algorithms. The data sequence has 10% randomly picked missing points. Linear curve fitting appears to recover both the frequency and the magnitude of the original frequency spectrum in Figure 5-13.

It is clear from the above four frequency plots that the Linear Curve Fitting method is the best as it not only recovers the exact frequency component but also the absolute energy of each frequency. The Mean Curve Fitting method is reasonably decent as it can recover the frequencies but not exactly the absolute energy of each frequency. The new DFT algorithm based on Stochastic averaging performs well for low frequency components but give erroneous result when the frequency gets larger. This is because of the data truncation that the algorithm does in order to keep the number of data points in each DFT calculation bock to be integer value. This drawback of the algorithm needs further improvement but the idea of stochastic averaging over the entire data sequence is better than the Linear Curve Fitting and Mean Curve Fitting methods, which only consider local information for averaging and estimation. Nevertheless, since the new DFT algorithm is fresh and not mature enough for immediate application, the Linear Curve Fitting method should be used instead for the time being to recover the missing HR data for driver monitoring. Future research work needs to be done to perfect the new algorithm.

The following frequency analysis result based on Linear Curve Fitting with 50% randomly missing point on the simulated HR data further supports the use of this ad hoc method for missing HR data processing.

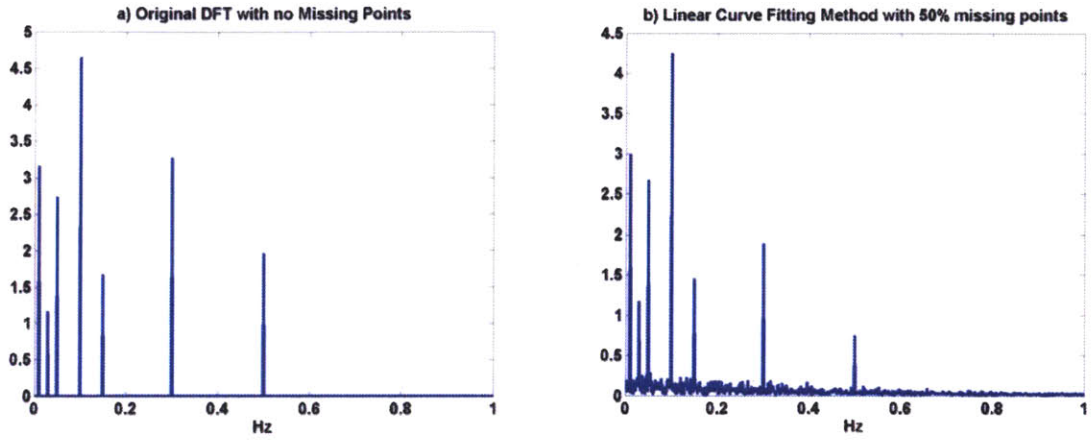

Figure 5-15: Comparison of frequency analysis of Linear Curve Fitting method for 50% missing data points

5.4 Ring Sensor Implementation and Road Test Result

5.4.1 Ring Sensor Implementation

Figure 5-16 shows a closed-up picture of the Ring Sensor and the picture of the Ring Sensor with data transfer cable. Figure 5-17 on the next page shows the Toyota Matrix used for road testing and the test setup inside the car.

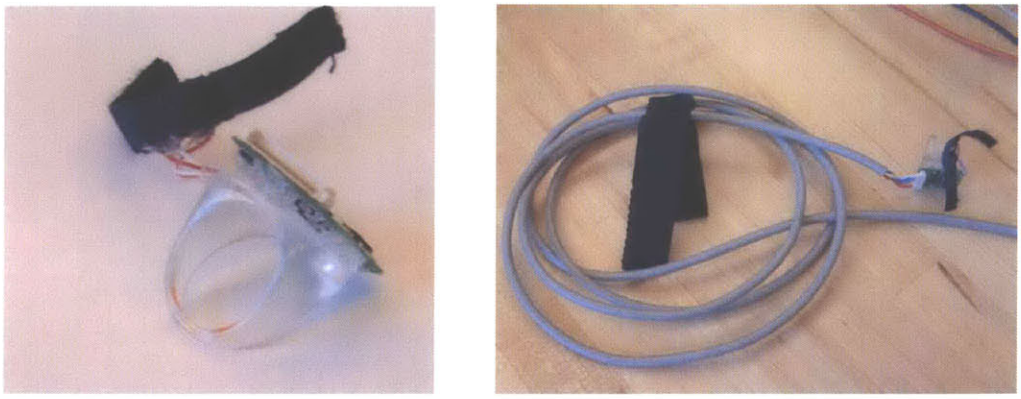

Figure 5-16: On the left: Close-up look at Ring Sensor and the sensor band; On the right: Ring Sensor setup with data transfer cable

Figure 5-17: Toyota Matrix used for road test and the actual test setup in the car

The Ring Sensor's specifications as well as the specifications for the peripherals are listed in the table below.

Table 5-1: Ring Sensor and Peripherals Specifications

Ring Sensor Specifications	
Voltage Supply	4.5V DC
Power Consumption (Typical)	100mW
Dimension	1.1"x 1" x 1.2"
Weight	≈10g
Peripherals Specifications	
Battery Pack	3 AA batteries
Battery Life (Typical)	30 hours
Ring Sensor Cable Type	9 Lead Coaxial
Ring Sensor Cable Length	2 m
Data Acquisition Card	NI DAQCard-6024E
Data Acquisition Box	NI SCB-68
Data Acquisition Cable	NI RC68-68
Data Acquisition System	Windows XP Professional
Data Acquisition Station	IBM Thinkpad T30
Data Acquisition Software	NI LabView 6.0i
Elastic Sensor Wrap	3M Nextcare No Hurt Tape

5.4.2 Road Test Data

The complete road test is performed on Highway 93 in Boston Metropolitan area. The Ring Sensor data was recorded continuously for 10 minutes and data processing was done offline with Matlab. The actual percentage of missing data is 30%. Linear Curve Fitting of the time sequence beat-to-beat HR data was performed first before the HRV is analyzed. The following is the overall HRV of the driver in the entire 10 minutes period.

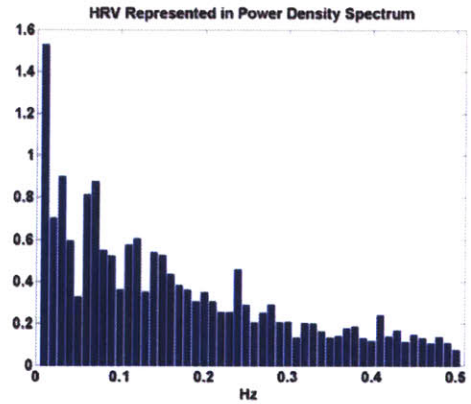

Figure 5-18: HRV analysis of the entire 10 minutes

In order to look at the change of the HRV over the 10 minutes period, six time sequences of 5 minutes each are individually analyzed in the following figure.

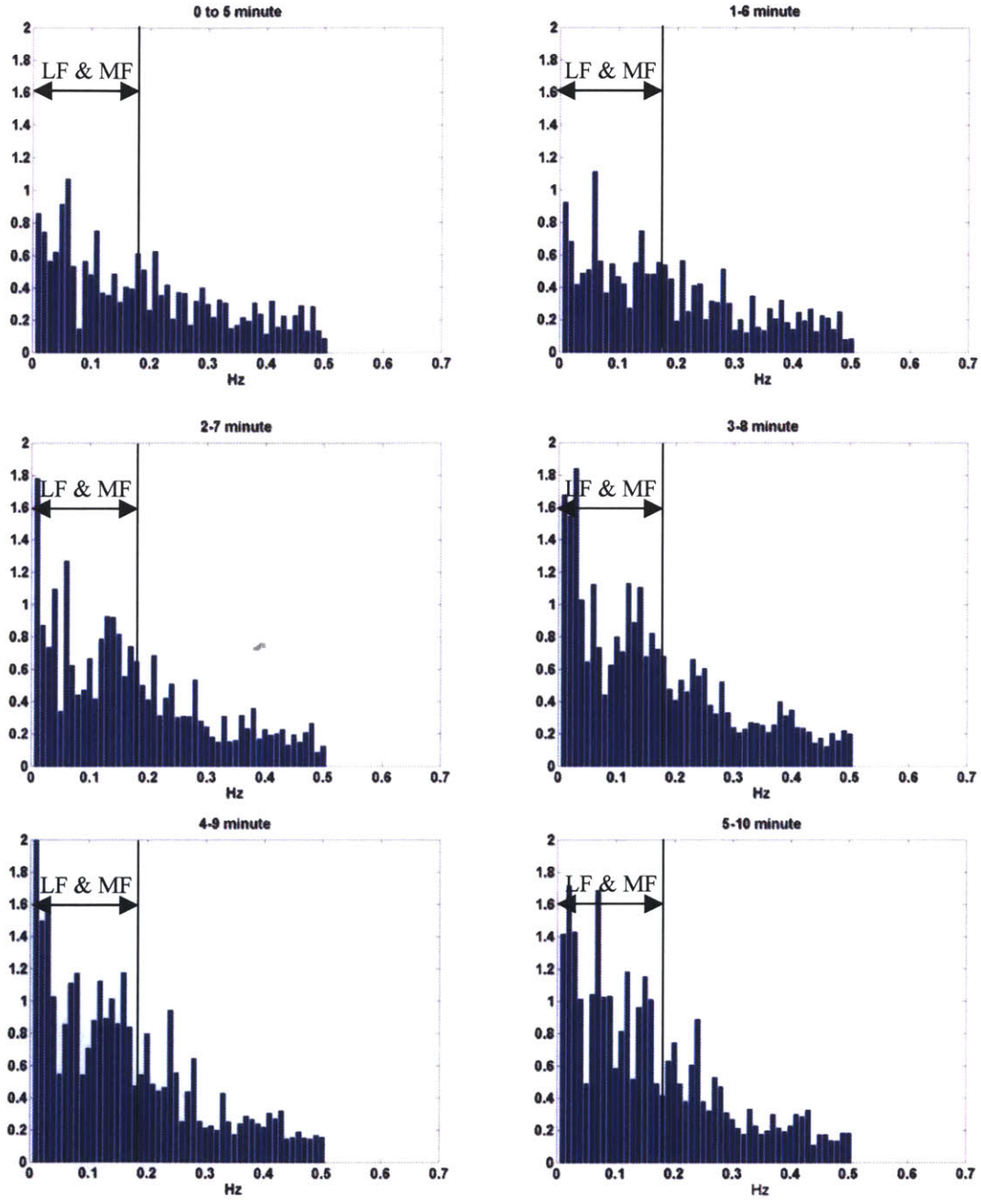

Figure 5-19: Six 5-minutes HR data sets are analyzed for the HRV trend

The driver started driving from the less populated town Newton, MA to Boston, MA. Along the road, the driver was experiencing increasing traffic and more winding roads. The HRV trend above clearly indicates the increase in the energy content of the LF (0.01-0.08Hz) and MF (0.08Hz-0.15Hz) region of the HRV as the driver approached heavier traffic. This road test result has confirmed the earlier conclusion on driver's *Mental Workload* as well as the validity of using the Ring Sensor for HRV measurement on the road.

5.5 Other Possible Ring Sensor Applications

With the success of eliminating the X-axis motion artifacts from the PPG signal using Adaptive Noise Cancellation, there are some other applications of the Ring Sensor that can be readily thought of. One typical application that can be verified in the lab environment is the monitoring the PPG signal of someone who is running. The hand motion associated with running is often the forward and backward swinging motion, which contains mainly motion in the X-axis defined in this thesis. The following figure shows how successfully this algorithm recovers the corrected PPG signal from a corrupted one obtained by the Ring Sensor attached to someone simulating the running hand motion. As can be seen below, this is clearly an success.

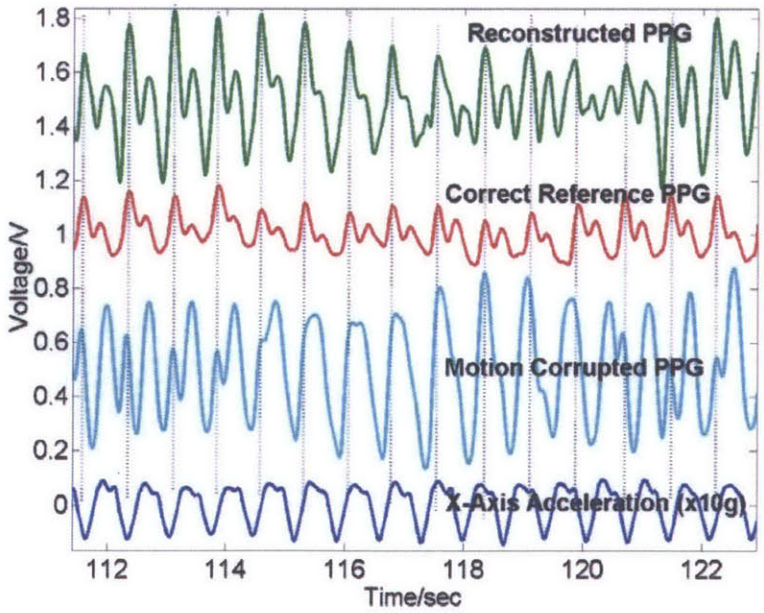

Figure 5-20: Comparing the reconstructed PPG with the correct reference PPG for running motion

6 CONCLUSION

Through extensive literature search, it has been found that there exists strong correlation between the Mental Workload of an automobile driver with his or her physiological measurements, especially the Heart Rate Variability (HRV) measurements. In order to make a driver's HRV monitoring on the road possible, a new photoplethysmograph (PPG) Ring Sensor prototype has been devised specifically for countering the problem of motion artifact that almost all wearable PPG sensors are facing. Most importantly, the motion artifacts on PPG signals caused by motion in the direction of blood flow in the digital arteries along the finger flanks have been eliminated using a customized Adaptive Noise Cancellation algorithm. Both the lab results and the road test results have suggested that the new Ring Sensor is indeed capable of rejecting motion artifacts in all three possible motion axes and producing considerable amount of usable beat-to-beat heart rate data on the road for HRV analysis. The problem of occasional missing data on the road has also been tackled with a suitable linear curve-fitting algorithm. Also, the sunlight saturation problem is dealt with using a simple DC averaging reference circuit. The final road test has proven the validity of the driver Mental Workload model and the validity of the Ring Sensor in monitoring the HRV of the driver on the road. Besides the application on driver monitoring, the Ring Sensor can also be used for other forms of wearable monitoring such as jogging.

The following summarizes the two major contributions that have been presented in this thesis

1. Motion-artifacts on the Ring Sensor's PPG signals due to motions in all three possible motion axes have been largely eliminated by using the local pressure setup and most importantly by using the Adaptive Noise Cancellation algorithm. For the Adaptive Noise Cancellation, only a time window of 10ms was found to be sufficient in reconstructing readable PPG waveforms. Moreover, it also ensures faster transition time for sudden motion and faster computation time.
2. Road test results confirm that the changes in the different frequency bands of the HRV spectrum are correlated to the changes in the driver's *Mental Workload* as described in various research papers on driver monitoring. Practical problems such as missing data points and sunlight saturation were also solved to make the road test data trustworthy.

7 APPENDIX

7.1 Circuit for the LED with Pulse-width Modulation Capability

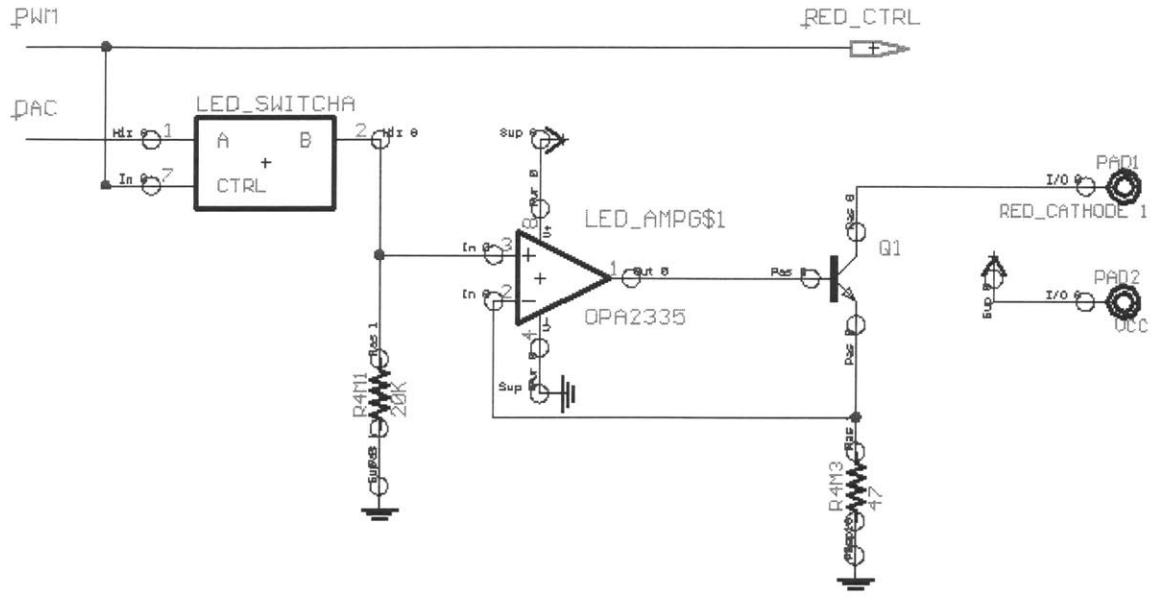

7.2 Circuit for obtaining signal and signal conditioning

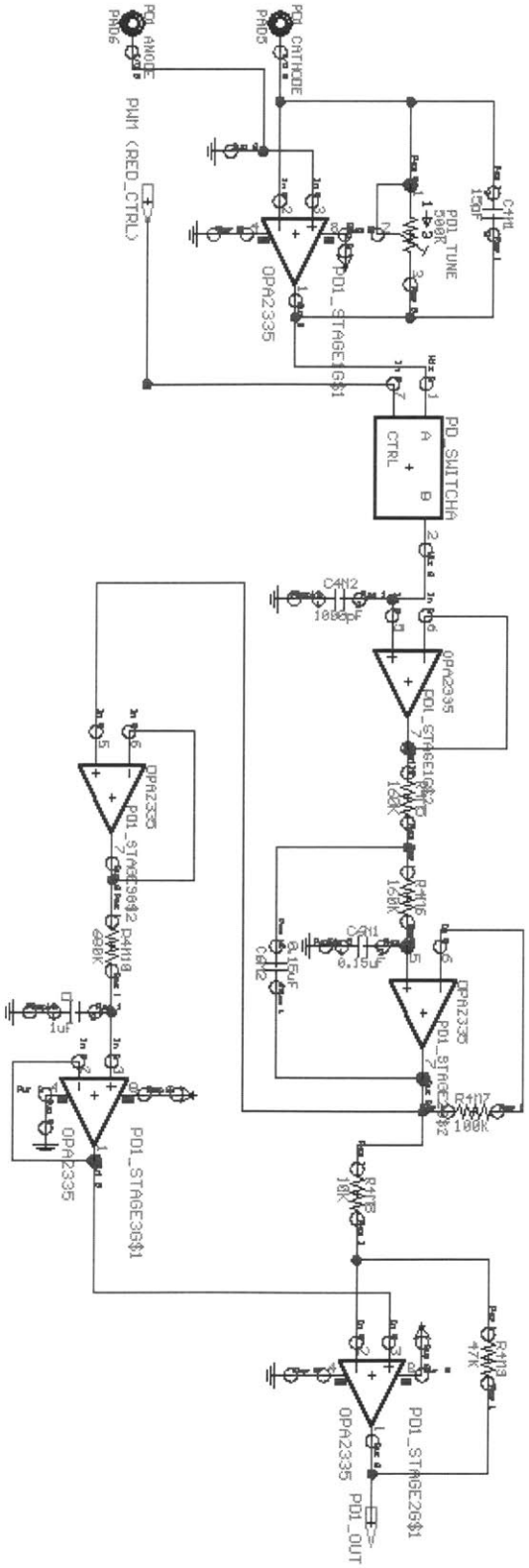

8 REFERENCES

1. J. R Treat, N. S. Tumbas, S. T. McDonald, D. Shinar, R. D. Hume, R. E. Mayer, R. L. Stanisfer and N. J. Castillan (1977) "Tri-level study of the causes of traffic accidents" Report No. DOT-HS-034-3-535-77, Indiana University
2. National Safety Council (1974) "Accident facts"
3. Marc Green and John W. Senders (1999) "Human Errors in Road Accidents", ERGO/GERO Human Factors Science
4. National Center for Statistics & Analysis, (1990-1999) "Crash Statistics"
5. I. M. McNally and M. Stone (2001) "Cross-Cultural Models of Road Traffic Accident Risk: Personality, Behavioral, Cognitive and Demographic Predictors", University of Central Lancashire, Preston, UK
6. National Highway Traffic Safety Admission, (1996) "Drowsy Driving and Automobile Crashes"
7. Yuji Takada and Osamu Shimoyama (2001) "Evaluation of Driving-Assistance Systems Based on Driver's Workload", Vehicle Research Laboratory, Nissan Research Center
8. Dick de Waard (1996) "The Measurement of Driver's *Mental Workload*", Center for Environmental and Traffic Psychology, University of Groningen.
9. Solange Akeselrod, David Gordon, F. Andrew Ubel, Daniel C. Shannon, A. Clifford Barger, Richard J. Cohen (1981) "Power Spectrum Analysis of Heart Rate Fluctuation: A Quantitative Probe of Beat-to-Beat Cardiovascular Control", Science, Volume 213, Issue 4504, 220-222
10. Rollin McCraty, Mike Atkinson, William A. Tiller, Glen Rein and Alan D. Watkins (1995) "The Effect of Emotions on Short-Term Power Spectrum Analysis of Heart Rate Variability, The American Journal of Cardiology, Volume 76
11. Zengyong Li (2002) "Spectral Analysis of Heart Rate Variability as a Quantitative Indicator of Driver Mental Fatigue", SAE 2002 World Congress & Exhibition
12. Redford B. Williams, James D. Lane, Cynthia M. Kuhn, William Melosh, Alice D. White and Saul M. Schanberg (1982) "Type A Behavior and Elevated Physiological and Neuroendocrine Responses of to Cognitive Tasks", Science, Volume 218, Issue 4571, 483-485

13. H. Harry Asada, Phillip Shaltis, Andrew Reisner, Sokwoo Rhee and Reginald Hutchinson (2003) "Wearable PPG-BioSensors ", IEEE Engineering in Medicine and Biology Magazine
14. Bernard Widrow, Robert C. Goodlin et al., "Adaptive Noise Canceling: Principles and Applications", Proceedings of the IEEE, vol. 63, pp. 1692-1716, Dec.1975
15. Oulun yliopiston kirjasto (2000) "Analysis of heart rate dynamics by methods derived from nonlinear mathematics: Clinical applicability and prognostic significance", Chapter 2.2